

Orientation and Transitions of Lyotropic Lamellar Phase under Shear

by

Haipeng Su

A thesis

presented to the University of Waterloo

in fulfilment of the

thesis requirement for the degree of

Master of Science

in

Physics

Waterloo, Ontario, Canada, 2014

© Haipeng Su 2014

AUTHOR'S DECLARATION

I hereby declare that I am the sole author of this thesis. This is a true copy of the thesis, including any required final revisions, as accepted by my examiners.

I understand that my thesis may be made electronically available to the public.

ABSTRACT

The intention of this study is to investigate the evolution and transition of lyotropic lamellar phase and the formation of multi-lamellar vesicles (MLVs) under shear flow, since the shear technology can be used to produce well defined multi-lamellar vesicles which are useful for encapsulating drugs in medical or research fields. The system was designed to stabilize and track one single multi-lamellar vesicle, which is being sheared under Couette shear flow between two co-rotational disks, by using polarizing microscope and a LabView program.

For the whole system, most parts of the hardware instrument and all the software programs were originally designed and homemade, which makes this a unique undertaking. Eighty percent of the time was spent on designing, assembling, testing and improving the hardware instrument and software programs to make sure the system can achieve our aim as accurately as possible.

The lyotropic lamellar phase sample is made of pentanol, dodecane, SDS and water. Nine different concentrations from 16% to 32% of SDS+Water were explored under five different shear rates from $3.3s^{-1}$ to $13.2s^{-1}$. Sodium dodecyl sulfate (SDS) is a kind of surfactant which has an amphiphilic molecular structure, and a certain liquid crystal structure (such as a lamellar phase) will be formed when it is dissolved in a water/oil mixture solvent.

It is a great achievement that one single multi-lamellar vesicle is able to be followed for over 20 minutes under shear, and it is found that the multi-lamellar vesicle does not exhibit any obvious changes with time once it was already formed. Three different structural regions were found for the dilute lamellar phase while evolving to the multi-lamellar vesicle orientation state under shear. However, only two regions were found for the lamellar phase with higher concentrations under low shear rate since the lamellar phase will not reach to the multi-lamellar vesicle state. Besides, on the basis of the results of these experiments, it can be concluded that either higher shear rate or higher concentration of SDS+Water will hasten the formation of multi-lamellar vesicles. For the transition time of reaching a uniform multi-lamellar vesicle orientation state, it can be reduced by increasing shear rate. In addition, the results show that the transition time is

decreasing more slowly for high concentrated lamellar phases than dilute lamellar phases with increasing the shear rate.

ACKNOWLEDGEMENTS

I would like to show my sincere appreciation to everyone who has inspired and helped me during my studies and research in the past few years. Without their kind-hearted and great support, I could never finish my Master degree in such a deep and advanced field.

First of all, I owe my greatest debt gratitude to my supervisor Professor Stefan Idziak, for his patient guidance, constant encouragement, and invaluable advice, no matter in my study or life. His brilliant ideas have led me into this interesting and exciting project, where I have gained a lot of priceless knowledge and experience with technologies. Professor Idziak is knowledgeable, enthusiastic, warm-hearted, and I always admire him for his personality, too. Besides, he has helped me a lot with my presentations, thesis writing, future planning and so on, and I do not think I can thank him enough.

Then, it is my extreme honor to thank Professor Jamie Forrest for being my committee member, Professor Bae-Yeun Ha for being my defense committee member, and Professor Hartwig Peemoeller for being both. I thank them very much for their valuable time and patience to listen to my immature presentations and awful spoken English. Their informative advice and suggestions showed a high inspiration to my research progress and results, and I could not have gone this far without their support.

Meanwhile, a very special thanks to Professor Stefan Idziak, the department of Physics and Astronomy, and the University of Waterloo. Because of their sufficient financial support, I can focus on my project with no worries. In addition, my thanks go to the university library where I can dig useful relevant academic materials and all the staff who were keen and kind-hearted to help with my requests.

Finally, I feel much indebted to my many friends who have favored me in my undergraduate and graduate study. I must thank Ph.D. student Kurt Schreiter who provided wonderful suggestions on the construction and improvement of my instrument set-up. I also need to acknowledge Ph.D. student Yu Chai for backing me up with his outstanding programming skills and thoughts. What's more, I doubt I will ever be able to convey my full gratitude to Ph.D.

candidate Qinrong Zhang for her magnificent favor on amending syntax error and semantic blurs in my thesis. And then I would like to give my particular thanks to Bingqing Yang and Hao Yan for their energetic motivation, and to all of my other friends for their nice encouragement.

Unfortunately, I am not able to list all the people that I want to appreciate in addition to my supervisor, committee members, the university, the faculty, my parents, my friends and so on, but their kindness and help will never be forgotten.

DEDICATION

To my beloved parents who have given me endless love and guided me to be whom I am now;

To my uncle Rui who has provided uncountable support and help on my life road;

To my unforgettable friends who have dispelled shadow and shine light in my heart;

To everyone who has appeared in my life, and the encounters that are driven by the destiny.

TABLE OF CONTENTS

List of Figures	x
List of Tables	xiii
I. Introduction	
1. Complex Fluid and Rheology	1
1-1 Background	1
1-2 Couette Shear Flow	1
1-3 Fluid Mechanics and Rheology Equations	3
1-4 Couette Shear Flow between Two Co-rotational Disks	8
2. Lyotropic Liquid Crystal and Lamellar Phase	10
2-1 Introduction to Liquid Crystal	10
2-2 Birefringence in Liquid Crystals	12
2-3 Lyotropic Lamellar Phase	13
3. Lyotropic Lamellar Phase under Shear	15
3-1 Water-Pentanol-Dodecane-SDS system	15
3-2 Defects in the Lamellar Phase	17
3-3 Multi-lamellar Vesicle	19
3-4 Orientation States of Lamellar Phase under Shear	20
II. Instrument and Program	
1. Shear Machine	23
1-1 AutoCAD Design of Shear Machine	23
1-2 The Field of View	27
1-3 Shear Rate Derivation	29
1-4 Actual Equipment	30
1-5 Simple Polarizing Microscope	31
2. LabView Program Interface	32
2-1 Front Panel of LabView Program	32
2-2 Stepper Motor Following Particle	34

2-3 Servo Motor Following Particle	35
3. Modification of Instrument and Program	36
4. Sample Preparation Procedure	38
5. Overall	38
III. Results	
1. Sample Preparation	40
2. Following one Single MLV under Microscope	41
2-1 MLV Observation by the Designed Equipment	42
2-2 One MLV versus Time under Shear	42
3. Lamellar Phase under Shear	43
3-1 Image Observations under Simple Polarization Microscope	43
3-2 Average Intensity Analysis	46
3-3 Fourier Transform Analysis	47
3-4 Transition Time for Different Samples under Various Shear Rates	53
3-5 Uncertainty of the Results	55
IV. Discussion	
1. Formation and Evolution of Multi-lamellar Vesicle	57
2. Transition Time for Lamellar Phase under Shear	57
3. Further Study	59
V. Conclusion	61
References	62
Appendix I – Flow Chart for the Logic of Stepper Motors Following Particle	64
Appendix II - Flow Chart for the Logic of Servo Motors Following Particle	65

LIST OF FIGURES

Figure-A1: The velocity profile between two parallel planes with the upper one sliding over the bottom one with a velocity of v_0	2
Figure-A2: Three kinds of Couette Flow	3
Figure-A3: Nine components of stress in three-dimensional flow	6
Figure-A4: a) Diagram of Couette shear flow between two co-rotational disks. b) The stress diagram for the element of the fluid between the co-rotational disks	9
Figure-A5: The velocity profile of the Couette shear flow between two co-rotational parallel disks with the same angular speed but opposite directions for a Newtonian Fluid	10
Figure-A6: Structures of Nematic and Smectic A liquid crystals constructed by rod-like molecules	11
Figure-A7: Demonstration of birefringence for an anisotropic material	12
Figure-A8: Demonstration of the birefringence property of liquid crystal	13
Figure-A9: The molecular structures of micelle and vesicles	14
Figure-A10: Molecular formula and structural formula of SDS, pentanol, and dodecane	15
Figure-A11: Ternary phase diagram of Water-Pentanol-Dodecane-SDS system for fixed ratio SDS: Water = 1: 1.55 at 21 °C	16
Figure-A12: a) The molecular structure of lamellar phase of Water-Pentanol-Dodecane-SDS system on carrying glass; b) Perfect lamellar phase with one dimensional positional ordered structure	16
Figure-A13: An edge dislocation defect in the lamellar phase	17
Figure-A14: Molecular structure of the edge dislocation in the lamellar phase	18
Figure-A15: a) A general defect in the lamellar phase with an unstrainght and curved defect surface. b) Molecular visual observation from the top	18
Figure-A16: A few dislocations in lamellar phase are observed between two crossed polarizers under an optical microscope	19
Figure-A17: Molecular structure of a multi-lamellar vesicle in a lyotropic solution.....	20

Figure-A18: a) Molecular structure for the cross section of one multi-lamellar vesicle observed from the top. b) Simulation observation of multi-lamellar vesicle between two crossed polarizers. c) Real patterns for multi-lamellar vesicles observed under microscope20
Figure-A19: Functional representation of orientation phase diagram for the Water-Pentanol-Dodecane-SDS lamellar system under shear21
Figure -B1: AutoCAD design for the shear machine between two co-rotational disks24
Figure-B2: The internal mechanics structure of the speed reducer for the servo motor26
Figure-B3: The field of view for the microscope27
Figure-B4: The relationship between the position of particle and the control of Servo motor or Stepper motor28
Figure-B5: Bird's eye view of the whole equipment for the shear machine and the controllers by eye30
Figure-B6: The actual shear machine we have for the experiments31
Figure-B7: The components and light path of the simple polarizing microscope from the shear machine32
Figure-B8: LabView program interface for controlling the motors and analyzing images33
Figure-B9: a) The velocity profile at an arbitrary time t_1 for co-rotational disks, and a particle is at the position p . b) The velocity profile after Δt time and particle moves to position p'35
Figure-B10: The front panel of modified LabView Program37
Figure-C1: X-ray diffraction patterns for samples with SDS+Water concentration of 16%, 20%, 24%, 28% and 32%41
Figure-C2: One large MLV with size of about 30 micrometers as seen under microscope42
Figure-C3: A series of images for the same MLV at different times43
Figure-C4: Images obtained for a 24% lyotropic lamellar phase under shear rate $5.0s^{-1}$ at different time within an hour44
Figure-C5: The image is taken at time $t = 50$ min, with a dimension of $0.44mm \times 0.33mm$45
Figure-C6: Average Intensity of Images for 24% Sample at five increasing shear rate46

Figure-C7: Fourier transform images for the corresponding raw images in Figure-C447
Figure-C8: Average pixel value along the same circle as a function of azimuthal angle for all the Fourier transform images48
Figure-C9: Average intensity distribution along the lines of constant azimuthal angle versus image number for 24% sample at shear rate $5.0s^{-1}$49
Figure-C10: Typical images represent the lamellar phase in three different regions50
Figure-C11: The Average pixel value along the ring for all Fourier transform images for 24% sample at various shear rates51
Figure-C12: Average intensity distribution along the lines versus time for 24% sample at various shear rates, obtained from Figure-G1151
Figure-C13: Average intensity distribution along the lines plot for 30% sample at shear rate $3.3s^{-1}$ and one typical image at <i>Region II</i>52
Figure-C14: The first transition time versus concentration of SDS+Water for different shear rates53
Figure-C15: The first transition time versus shear rate for different concentrated samples54
Figure-C16: The plots of the second transition time against both: concentration of SDS+Water, and shear rate54
Figure-C17: The plots of the time interval for <i>Region II</i> against both: concentration of SDS+Water, and shear rate55

LIST OF TABLES

Table -D1: Prepared samples for the experiment according to the ternary phase diagram40

Table-D2: Transition times for samples with 16% and 24% of SDS+Water in two trials56

I. INTRODUCTION

1. Complex fluids and Rheology

1-1 Background

Fluids can be classified into Newtonian fluids or non-Newtonian fluids in terms of the dependence of the viscosity on shear rate. A Newtonian fluid is recognized as a kind of fluid whose viscosity is independent of shear rate, which means the ratio of shear stress to shear rate is constant at a given temperature. For example: water, ethanol, benzene and all gases are identified as Newtonian fluids [2]. All fluids that don't follow the linear relation between shear stress and shear rate are defined as non-Newtonian fluids. Fluids such as slurries, emulsions, pastes and other mixtures are all typical non-Newtonian fluids.

Among the non-Newtonian fluids, some are called shear-thinning fluids (also known as pseudo-plastic fluids) for which the viscosity decreases with the increase of shear rate. Others are shear-thickening fluids, which are less common than shear-thinning fluids [17]. Fluids such as nail polish, syrup and paint are common shear-thinning fluids.

One particular kind of non-Newtonian fluid that will flow only when the shear stress is greater than a critical value known as the 'yield stress' is called a visco-plastic (or 'yield stress') fluid. To give an example: toothpaste, mayonnaise and ketchup which will not flow out of containers unless enough pressure is applied are commonly used in our daily life [1]. A Visco-plastic fluid exhibits some characteristics of both an ideal fluid and an elastic solid [3].

To explore the rheological properties of a complex fluid as a function of shear rate, a technology called 'shearing flow' is introduced to achieve that goal.

1-2 Couette Shear Flow

Shear flow in fluid dynamics can be generally defined as the flow movement caused by shear stress in gradient, where the shear stress is the unit of applied force over the cross sectional area. There are different types of shear flow in rheology, and the fundamental type called simple steady shear flow can be described as the flow of fluid between two infinite parallel planes with

one plane moving over another. The velocity profile for a Newtonian fluid is shown in Figure-A1.

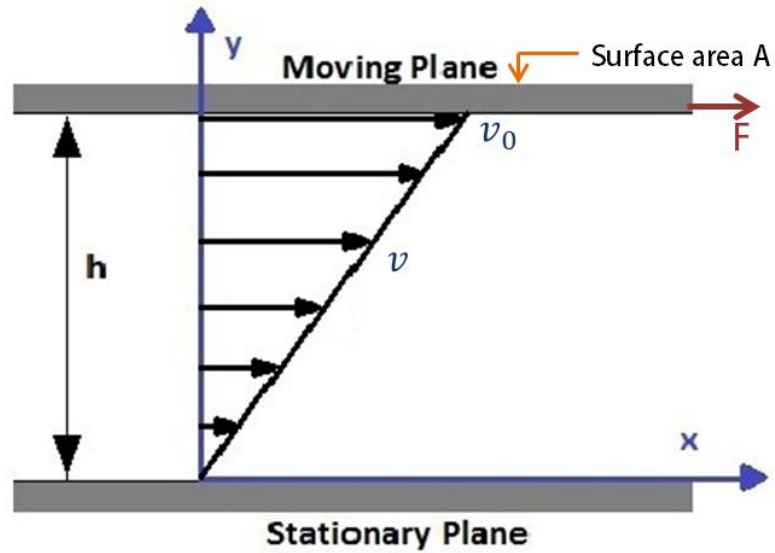


Figure-A1: The velocity profile between two parallel planes with the upper one sliding over the bottom one with a velocity of v_0 .

For an incompressible Newtonian fluid flowing between two parallel infinite planes, the velocity of a fluid element in the direction that is perpendicular to the plane is a linear function with the distance to the moving plane, and we have,

$$\dot{\gamma} = \frac{v}{h} = \frac{dv}{dy}, \quad \text{where } \dot{\gamma} \text{ is the velocity gradient, or the shear rate.}$$

and

$$\tau = \eta \dot{\gamma} = \eta \frac{dv}{dy}, \quad \text{where } \tau \text{ is the shear stress and } \eta \text{ is defined as}$$

the viscosity at a given time.

For a general flowing fluid, the shear stress is,

$$\tau = \frac{F}{A}, \quad \text{where } F \text{ is the applied force, and } A \text{ is the cross – section area.}$$

The viscosity of a fluid measures its resistance to the relative movement between layers. Depending on the viscosity, fluids can be commonly described as either thick or thin [12].

Couette flow is described as the kind of shear flow where one plane is moving relative to another parallel plane [18], and it produces the velocity profile as shown in Figure-A1. In Figure-A2, three geometries that can produce Couette shear flow are presented.

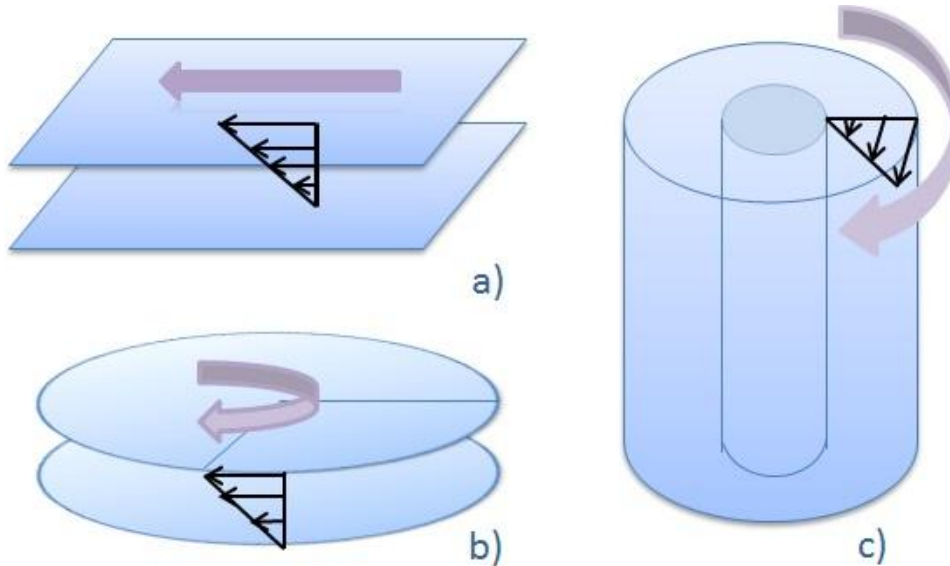


Figure-A2: Three kinds of Couette Flow. a) The Plane Couette Flow occurs between two infinite parallel planes; b) The Torsional Couette Flow occurs between two parallel disks; c) The Cylinder Couette Flow occurs between two concentric cylinders.

Basically, we can set up simple equipment based on the Couette Flow of a fluid to achieve the lamellar shearing flow, and then measure the shear rate corresponding to different shear stress. Conversely, we can measure the resulting shear stress based on the shear rate to obtain the viscosity for the fluid.

1-3 Fluid Mechanics and Rheology Equations

Since fluids show entirely different behaviors in motion when compared to solids, we cannot use classical mechanics for solids to describe the motion of a complex fluid. The field of rheology was born to explore complex fluids. To approach the problems related to flowing fluids, rheology can be characterized by three principles: the Conservation of Mass, Newton's Law of Motion, and the Conservation of Energy in mechanics, which give us three

corresponding equations in fluid: the Continuity Equation, the Momentum equation, and the Energy Equation [2].

For a general flowing fluid, the velocity will have three components $\vec{v} = (v_x, v_y, v_z)$, and each component is varying along three directions $\vec{r} = (x, y, z)$. To better describe the velocity, a four-dimensional vector is introduced to describe the velocity variation of a fluid element in different directions at an instant of time $\vec{v} = \vec{v}(x, y, z, t)$.

Continuity equation

The conservation of mass in mechanics implies that the decrease of mass in a certain volume is equal to the outflow mass [27]. The mass flux per unit area in each direction is ρv_i , where ρ is the density, and i can be x, y, z . Therefore, for an infinitesimal element with dimensions dx, dy, dz in the fluid, we have,

$$\frac{\partial(\rho v_x)}{\partial x} + \frac{\partial(\rho v_y)}{\partial y} + \frac{\partial(\rho v_z)}{\partial z} = -\frac{\partial \rho}{\partial t} \quad (1)$$

or

$$\nabla \cdot (\rho \vec{v}) = -\frac{\partial \rho}{\partial t} \quad (2)$$

and this is the general form of the continuity equation.

If the fluid is incompressible and under steady shear flow, the density ρ will be independent of position and time, so $\frac{\partial \rho}{\partial x} = \frac{\partial \rho}{\partial y} = \frac{\partial \rho}{\partial z} = 0$ and $\frac{\partial \rho}{\partial t} = 0$. Then the continuity equation becomes,

$$\nabla \cdot \vec{v} = \frac{\partial v_x}{\partial x} + \frac{\partial v_y}{\partial y} + \frac{\partial v_z}{\partial z} = 0 \quad (3)$$

Momentum equation

Based on the momentum formula in classical mechanics,

$$\Delta p = F \cdot \Delta t = m \cdot a \cdot \Delta t$$

where Δp is the change of momentum, F is the external force, a is the acceleration and Δt is the time interval.

Now consider an infinitesimal element of fluid, with mass $\rho dx dy dz$, and velocity of components $v_i = v_i(x, y, z, t)$. We have,

$$dv_i = \frac{\partial v_i}{\partial x} dx + \frac{\partial v_i}{\partial y} dy + \frac{\partial v_i}{\partial z} dz + \frac{\partial v_i}{\partial t} dt, \quad \text{with } i = x, y, z.$$

Taking the derivative of v_i with respect to time t , we have,

$$\frac{dv_i}{dt} = \frac{\partial v_i}{\partial x} \cdot \frac{dx}{dt} + \frac{\partial v_i}{\partial y} \cdot \frac{dy}{dt} + \frac{\partial v_i}{\partial z} \cdot \frac{dz}{dt} + \frac{\partial v_i}{\partial t}$$

with

$$v_x = \frac{dx}{dt}, \quad v_y = \frac{dy}{dt}, \quad v_z = \frac{dz}{dt}$$

We finally get,

$$\frac{dv_i}{dt} = v_x \frac{\partial v_i}{\partial x} + v_y \frac{\partial v_i}{\partial y} + v_z \frac{\partial v_i}{\partial z} + \frac{\partial v_i}{\partial t}$$

or

$$\frac{dv_i}{dt} = \vec{v} \cdot (\nabla \cdot v_i) + \frac{\partial v_i}{\partial t}, \quad \text{with } i = x, y, z.$$

Therefore, the inertial force F_{I_i} is

$$F_{I_i} = m \frac{dv_i}{dt} = \left[\vec{v} \cdot (\nabla \cdot v_i) + \frac{\partial v_i}{\partial t} \right] \cdot \rho \cdot dx dy dz \quad (4)$$

Reconsidering the fluid element, the external forces come from the gravitational field and the stress [2]. If the fluid element has a gravitational potential function V referenced to a zero plane, then the force due to gravity G_i is

$$G_i = -\rho \frac{\partial V}{\partial i} dx dy dz, \quad \text{with } i = x, y, z. \quad (5)$$

The stress is a combination of two parts, the normal stress due to the pressure and the shear stress because of the viscosity. Figure-A3 shows the stress diagram of a fluid element in a three-dimensional flow [3] (totaling 9 components), with 3 components of normal stress and 6 components of shear stress.

The indices of the 6 shear stresses $\tau_{xy}, \tau_{yx}, \tau_{xz}, \tau_{zx}, \tau_{yz}, \tau_{zy}$ indicate the plane where the stress is acting on and the direction in which the stress is pointing [2]. For example, τ_{xy} is the shear stress acting on the plane that is perpendicular to the x axis and pointing in the y direction. The shear stresses are not totally independent with each other because $\tau_{xy} = \tau_{yx}$, $\tau_{xz} = \tau_{zx}$, $\tau_{yz} = \tau_{zy}$ [2].

According to the mechanics equation $F = \text{pressure} \cdot \text{area}$, we can get the stress force in x direction,

$$F_x = \left(\frac{\partial p_{xx}}{\partial x} + \frac{\partial \tau_{xy}}{\partial y} + \frac{\partial \tau_{xz}}{\partial z} \right) \cdot dx dy dz \quad (6)$$

Under this circumstance, *inertial force = gravity force + stress force*, and combining equations (4), (5) and (6), for x component, we can get,

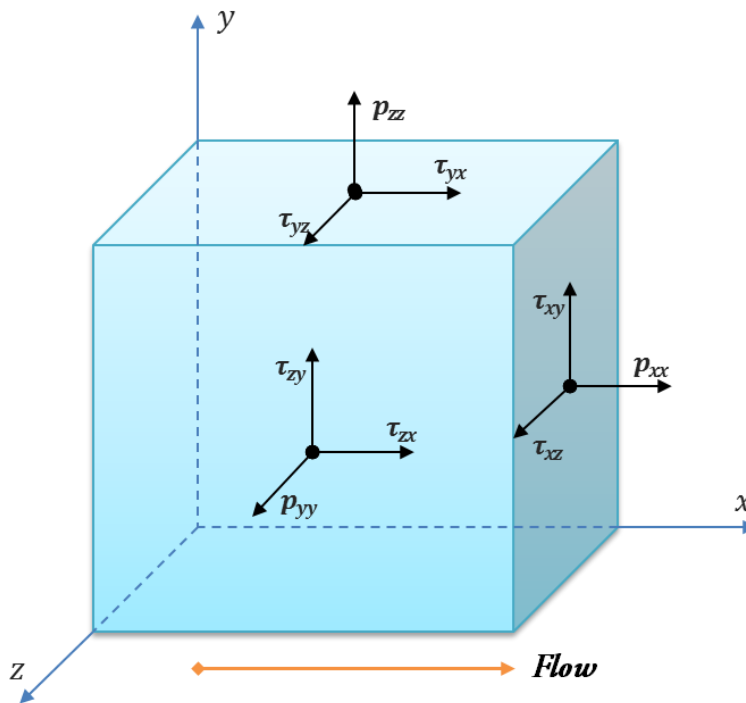


Figure-A3: Nine components of stress in three-dimensional flow.

$$\rho \frac{dv_x}{dt} \cdot dx dy dz = -\rho \frac{\partial v}{\partial x} \cdot dx dy dz + \left(\frac{\partial p_{xx}}{\partial x} + \frac{\partial \tau_{xy}}{\partial y} + \frac{\partial \tau_{xz}}{\partial z} \right) \cdot dx dy dz \quad (7)$$

and this becomes the momentum equation containing stress for the x component,

$$\frac{dv_x}{dt} = -\frac{\partial V}{\partial x} + \frac{1}{\rho} \left(\frac{\partial p_{xx}}{\partial x} + \frac{\partial \tau_{xy}}{\partial y} + \frac{\partial \tau_{xz}}{\partial z} \right) \quad (8)$$

Since the normal stress is related to the strain and the shear stress is related to the velocity,

$$\begin{cases} \tau_{xy} = \tau_{yx} = \eta \left(\frac{\partial v_x}{\partial y} + \frac{\partial v_y}{\partial x} \right) \\ \tau_{xz} = \tau_{zx} = \eta \left(\frac{\partial v_x}{\partial z} + \frac{\partial v_z}{\partial x} \right) \\ \tau_{yz} = \tau_{zy} = \eta \left(\frac{\partial v_y}{\partial z} + \frac{\partial v_z}{\partial y} \right) \end{cases} \quad (9)$$

Also, Hooke's law [2] gives us the formula of isotropic stress p in the fluid,

$$p_{xx} = -p + \frac{2}{3}\eta \left(2\frac{\partial v_x}{\partial x} - \frac{\partial v_y}{\partial y} - \frac{\partial v_z}{\partial z} \right) \quad (10)$$

Substitute the stress formulas (9) and (10) back into equation (8), we can get the general expression of the momentum equation in terms of pressure, velocity and viscosity,

$$\frac{dv_x}{dt} = -\frac{1}{\rho} \frac{\partial p}{\partial x} - \frac{\partial V}{\partial x} + \frac{\eta}{\rho} \left[\nabla^2 v_x + \frac{1}{3} \frac{\partial}{\partial x} \left(\frac{\partial v_x}{\partial x} + \frac{\partial v_y}{\partial y} + \frac{\partial v_z}{\partial z} \right) \right] \quad (11)$$

or a general form for the x, y, z components,

$$\frac{dv_i}{dt} = -\frac{1}{\rho} \frac{\partial p}{\partial i} - \frac{\partial V}{\partial i} + \frac{\eta}{\rho} \left[\nabla^2 v_i + \frac{1}{3} \frac{\partial}{\partial i} (\nabla \cdot \vec{v}) \right], \text{ with } i = x, y, z. \quad (12)$$

Then for an incompressible fluid ($\frac{\partial \rho}{\partial i} = 0$) under steady shear ($\nabla \cdot \vec{v} = 0$), the momentum equation becomes,

$$\frac{d\vec{v}}{dt} = -\frac{1}{\rho} \frac{\partial p}{\partial i} - \frac{\partial V}{\partial i} + \frac{\eta}{\rho} \nabla^2 \cdot \vec{v} \quad (13)$$

Equation (13) is known as the Navier-Stokes equation [25].

Energy equation

For an incompressible fluid in steady and friction flow, the energy equation is given as the Bernoulli equation [29],

$$\frac{p}{\rho g} + V + \frac{v^2}{2g} = E = \text{constant} \quad (14)$$

where E is the total mechanical energy for every infinitesimal element in the fluid.

1-4 Couette Shear Flow between Two Co-rotational Disks

Consider a Couette shear flow with two co-rotational parallel disks with the same angular speed but opposite directions. If the speed of the rotating disks is very slow and the radius is big enough compared to the gap, we can assume that there is no movement in the radial \hat{r} direction. Also the infinitesimal fluid element will be under steady shear flow between two horizontal infinite parallel planes with a separation d .

Then we have a few conditions:

- 1) Steady flow in \hat{x} direction gives,

$$\frac{\partial v}{\partial x} = 0 \quad \& \quad v = v(y)$$

- 2) Boundary conditions at the top and bottom disks are,

$$\begin{cases} \text{at } y = 0, & v(y) = -\omega r \\ \text{at } y = d, & v(y) = +\omega r \end{cases}$$

where r is the distance to the center of the disk, and ω is the angular velocity of each disk.

- 3) No change of momentum in \hat{x} direction implies,

$$F_x = 0$$

For an infinitesimal element in the flow, if we suppose that the pressure at the left is p , the shear stress at the top is τ . We can get the stress diagram in Figure-A4.

Then we have,

$$\begin{aligned} F_x = 0 &= F_{Top} + F_{Bottom} + F_{Right} + F_{Left} \\ &= \tau dxdr - \left(\tau - \frac{\partial \tau}{\partial y} dy \right) dxdr + p dydr - \left(p + \frac{\partial p}{\partial x} dx \right) dydr \\ &= \frac{\partial \tau}{\partial y} dy dx dr - \frac{\partial p}{\partial x} dx dy dr = 0 \end{aligned}$$

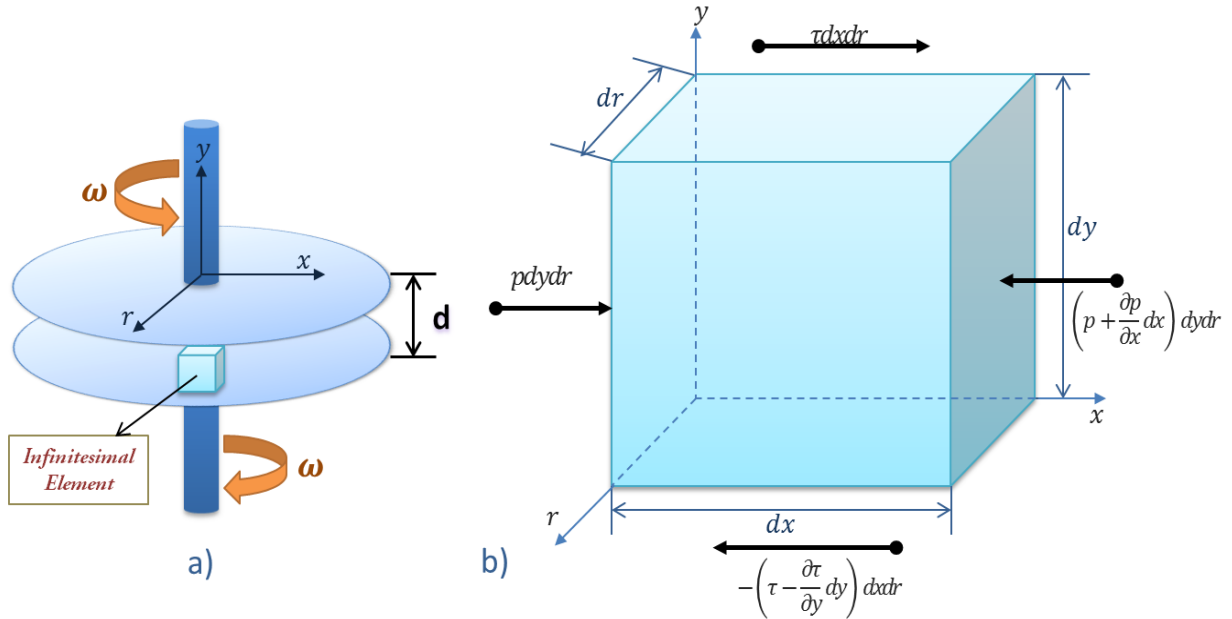


Figure-A4: a) Diagram of Couette shear flow between two co-rotational disks. Both disks have the same angular speed but opposite directions. b) The stress diagram for the element of the fluid between the co-rotational disks.

Therefore,

$$\frac{\partial \tau}{\partial y} = \frac{\partial p}{\partial x} \Rightarrow \int \frac{\partial \tau}{\partial y} = \int \frac{\partial p}{\partial x}$$

$$\Rightarrow \tau = \int \frac{\partial p}{\partial x} dy \Rightarrow \tau = \frac{\partial p}{\partial x} \cdot y + C_1$$

Recalling the relation between shear stress and viscosity $\tau = \eta \frac{\partial v}{\partial y}$, we have,

$$\frac{\partial v}{\partial y} = \frac{1}{\eta} \frac{\partial p}{\partial x} y + \frac{C_1}{\eta} \quad (15)$$

$$v(y) = \frac{1}{\eta} \frac{\partial p}{\partial x} \cdot \left(\frac{1}{2} y^2\right) + \frac{C_1}{\eta} \cdot y + C_2 \quad (16)$$

Applying the boundary conditions,

$$\begin{cases} v(y=0) = C_2 = -\omega r \\ v(y=d) = \frac{1}{2\eta} \frac{\partial p}{\partial x} y^2 + \frac{C_1}{\eta} \cdot y + C_2 = \omega r \end{cases} \quad (17)$$

$$\Rightarrow \begin{cases} C_1 = \frac{2\omega r \eta}{d} - \frac{d}{2} \left(\frac{\partial p}{\partial x} \right) \\ C_2 = -\omega r \end{cases} \quad (18)$$

Combining (16) and (18), we have,

$$v(y) = \frac{1}{2\eta} \frac{\partial p}{\partial x} \cdot y^2 + \left(\frac{2\omega r}{d} - \frac{d}{2\eta} \frac{\partial p}{\partial x} \right) \cdot y - \omega r \quad (19)$$

Since the zero pressure gradient is obtained $\frac{\partial p}{\partial x} = 0$ from the Couette shear flow, we can derive the velocity profile:

$$v(y) = \frac{2\omega r}{d} y - \omega r \quad (20)$$

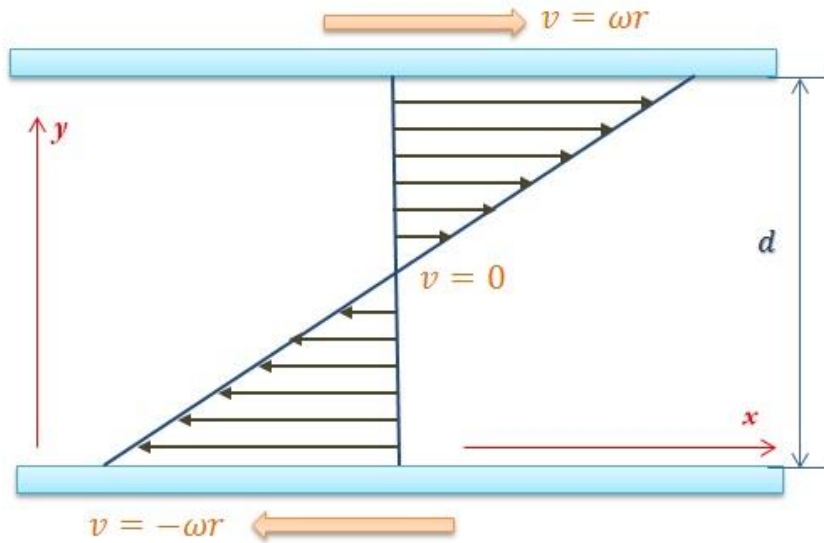


Figure-A5: The velocity profile of the Couette shear flow between two co-rotational parallel disks with the same angular speed but opposite directions for a Newtonian Fluid.

As shown in Figure-A5, this velocity profile is only for Newtonian fluid under steady shear flow, but even for non-Newtonian fluid, there is also one layer where the velocity is zero.

2. Lyotropic Liquid Crystal and Lamellar Phase

2-1 Introduction to Liquid Crystal

In 1888, a transition to a cloudy liquid was discovered by Friedrich Reinitzer, a botanist, when

he was melting cholesterol at 145.5°C [11]. This new matter was observed to have the property of birefringence, and was named “liquid crystal” to differentiate it from being neither a pure solid nor liquid [1]. Since the liquid crystal resides in an intermediate phase between liquid and crystalline, it possesses flow properties from liquids; and uncompleted positional or orientational characteristics from solids.

Among the different types of liquid crystals, Nematic and Smectic A are the two most basic phases, as shown in Figure-A6, in which the arrow \hat{n} is the preferred direction of orientation for the rod-like molecules, and it is called the ‘director’ [10].

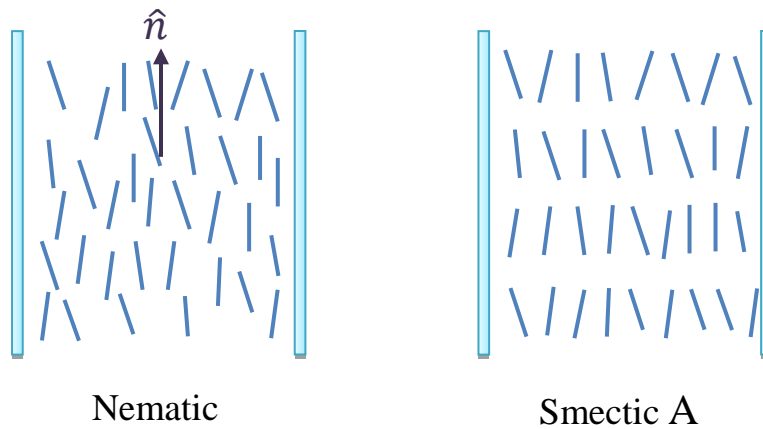


Figure-A6: Structures of Nematic and Smectic A liquid crystals constructed by rod-like molecules. Notation \hat{n} represents the director.

For the Nematic phase, the rod-like molecular structure only has orientational order, which means the molecules are constrained to orient themselves towards a certain direction, but no positional order. As to the Smectic A phase, the rod-like molecules possess both orientational order and one-dimensional (or layered) positional order. In pure solids, molecules are constrained to occupy certain positions in three dimensions.

It was discovered that disk-like molecules can also form liquid crystals, and they are called discotic liquid crystals, among which the columnar phase has a two-dimensional ordered positional structure like a set of stacked coins [10]. The Chiral liquid crystal, which presents some spectacular optical properties, also exists in discotic liquid crystalline form.

2-2 Birefringence in Liquid Crystals

In general optics, if we send a beam of light with x and y polarizations to an anisotropic material, two polarized rays will travel along two different paths because of their unequal refraction indexes of each polarization. This phenomenon is known as birefringence [10], and Figure-A7 demonstrates the light path.

The birefringence property of liquid crystals is the consequence of the optical anisotropy of the rod-like molecule, which causes the velocity difference and phase difference between two light beams whose polarizations are perpendicular and parallel to the director respectively [14]. This special characteristic can be easily observed and explained by using two crossed polarizers.

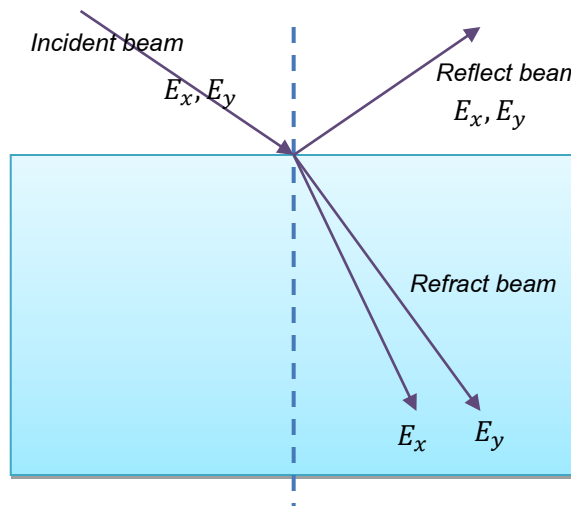


Figure-A7: Demonstration of birefringence for an anisotropic material.

If we put an isotropic material between two crossed polarizers, all light transmitted through the first polarizer will be completely blocked by the second polarizer since the isotropic material will not change the polarization of light, and we will see darkness after the second polarizer. However, when a liquid crystal is placed between two crossed polarizers, if the linear polarized light passing through the first polarizer has an angle between 0° to 90° with respect to the director of the liquid crystal, it will be separated into two polarized beams after transmitting through the material. One polarization will be in the same direction of the director and the other will be perpendicular to the director. Also, these two beams will have a phase difference because the velocities in the liquid crystal are different. Both beams will emerge from the

second polarizer, and we can see brightness after. A demonstration is shown in Figure-A8.

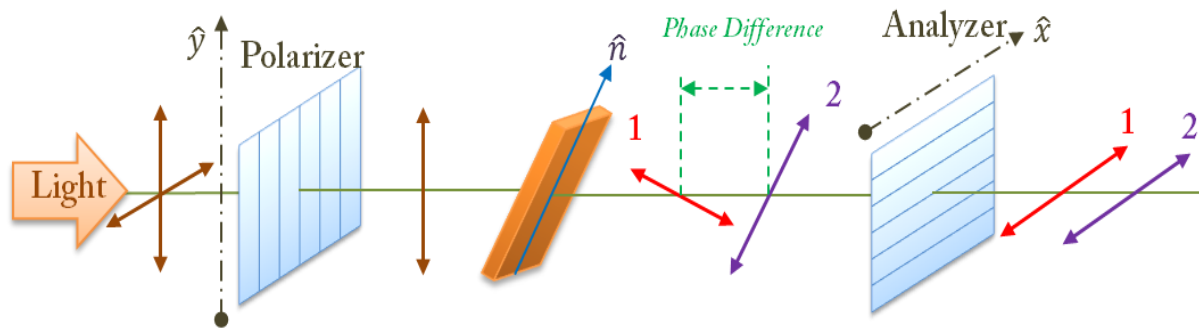


Figure-A8: Demonstration of the birefringence property of liquid crystal. Notation \hat{y} , \hat{n} , \hat{x} represents: the polarization of the first polarizer, the direction of the director, and the polarization of the second analyzer, respectively. Double arrows represent the polarization of lights. Two linear polarized lights are produced after the liquid crystal. Light 1 and light 2 are perpendicular and parallel to the director respectively. Both light 1 and light 2 will partly emerge from the analyzer, and we will see brightness.

Two particular circumstances that should be noted are: the linear polarized beam that comes from the first polarizer is either perpendicular or parallel to the director. Under these circumstances, the liquid crystal will not rotate the polarization and no light will emerge from the latter polarizer [10]. Some visual observations for the liquid crystal between crossed polarizers under the microscope will be discussed later.

2-3 Lyotropic Lamellar Phase System

One special class of liquid crystal is a mixture that is made of two or more components, especially surfactants and solvents, where the phase or structure are dependent on the concentration of components [1]. These mixtures are called lyotropic liquid crystals. Like other liquid crystals, lyotropic liquid crystals are also very important to scientific and technological fields.

A typical material called surfactant is a kind of substance where the molecules are amphiphilic and always have 'heads' and 'tails', which are hydrophilic and hydrophobic groups, respectively [26]. The consequence of the combination of water-loving heads and oil-loving tails is that these amphiphilic molecules will self-assemble into aggregates with various size and structures.

A very small amount of surfactant can totally dissolve into water or oil without forming a certain structure, since it is possible for all molecules to mix into the solvent evenly [1]. Then with the increase of concentration of amphiphilic molecules, the mixture reaches the critical micelle concentration, with two fundamental constructions forming called micelles and vesicles [26], as shown in Figure-A9.

These structures are stable since hydrophilic groups are in contact with water molecules outside of the micelles or vesicles, while the hydrophobic groups are pointing inside and stacking onto each other. Reversed structures that can also be assembled when amphiphilic materials dissolves into oil, since water-loving heads are pointing inside and oil-loving tails are in contact with the outside oil. Then, for a higher concentration of amphiphilic material, different liquid crystalline phases will be aggregated.

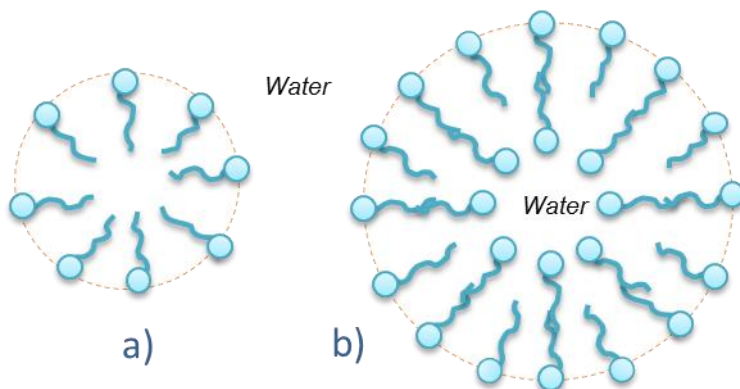


Figure-A9: The molecular structures of micelle and vesicles that are formed when amphiphilic materials are dissolving in water at a low concentration.

Two main structures that formed are called the lamellar phase and hexagonal phase. The lamellar phase is made of planar bilayers formed by amphiphilic molecules and separated by water from each layer. This structure will be discussed later. The d-spacing of the lamellar phase is defined as the summation of the thickness of one bilayer and the separation between two bilayers.

This lyotropic lamellar phase is a undoubtable liquid crystal structure with the property of rotational order and layered positional order from crystal; and the property of viscosity from fluids [4].

In the past years, many membrane systems have been studied and it has been found that the orientation of lamellar phase, as well as the formation and evolution of multi-lamellar vesicles can be influenced by shear rate [9]. In different regimes of shear rate, the original lamellar phase solution will show us a transition among several different orientation states.

3. Lyotropic Lamellar Phase under Shear

3-1 Water-Pentanol-Dodecane-SDS system

One lamellar system which was made of water, sodium dodecyl sulfate (SDS), pentanol and dodecane was studied in the past by using different techniques, such as: light scattering [4], neutron scattering [16], microscopic observation [5], and dielectric measurements [15]. The chemical molecular structures of the components are briefly shown in Figure-A10.

In Water-Pentanol-Dodecane-SDS systems, the lyotropic lamellar phase can remain stable in a solution with very low and very high concentration of surfactant, which will produce various d-spacing from tens to hundreds of Angstroms between two membranes [4]. This is the reason why we chose this special system to prepare lamellar phase. The phase diagram is shown in Figure-A11.

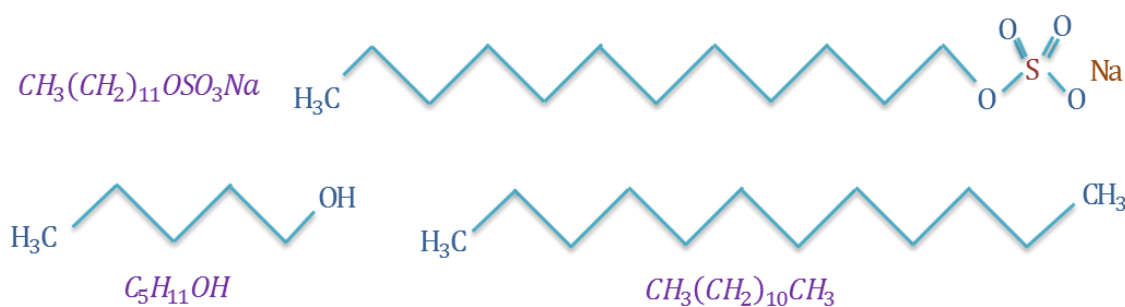


Figure-A10: Molecular formula and structural formula of SDS ($CH_3(CH_2)_{11}OSO_3Na$), pentanol ($C_5H_{11}OH$), and dodecane ($CH_3(CH_2)_{10}CH_3$).

Based on the percentage of each component, multiple phases L_2 , D , L_1 and E are discovered to be either Isotropic, Lamellar, Sponge or Hexagonal phases [21]. According to the phase diagram for the above solution, we can prepare a lamellar phase dilute solution or concentrated solution

depending on the percentage of dodecane solvent.

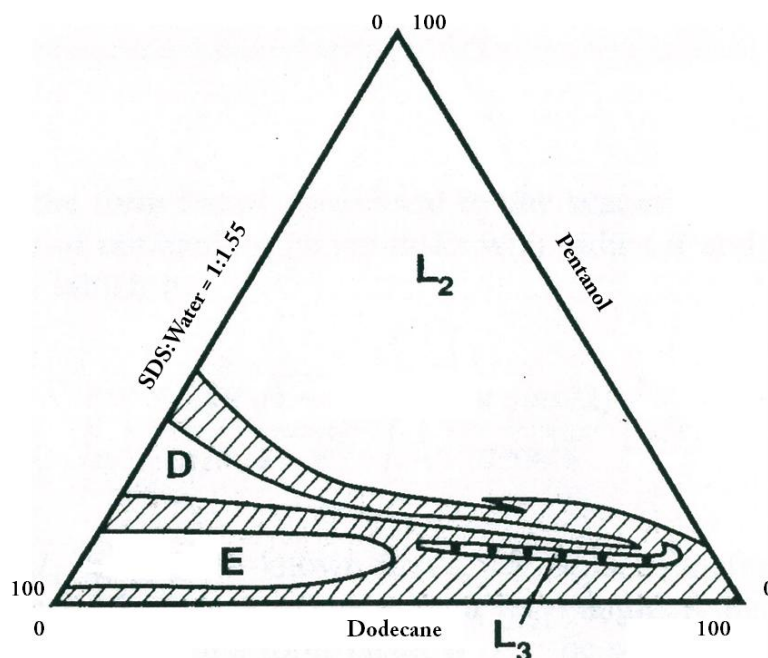


Figure-A11: Ternary phase diagram of Water-Pentanol-Dodecane-SDS system for fixed ratio SDS: Water = 1: 1.55 at 21 °C [Redrawn from Diat O., Roux D., J. Phys. II France 3, 1428 (1993)], and region D represents the lamellar phase.

For the lamellar phase in Water-Pentanol-Dodecane-SDS solution, the membrane is constructed by pentanol, SDS and water, and the solvent is dodecane, as shown in Figure-A12. The membranes are ordered among layers but disordered within each layer.

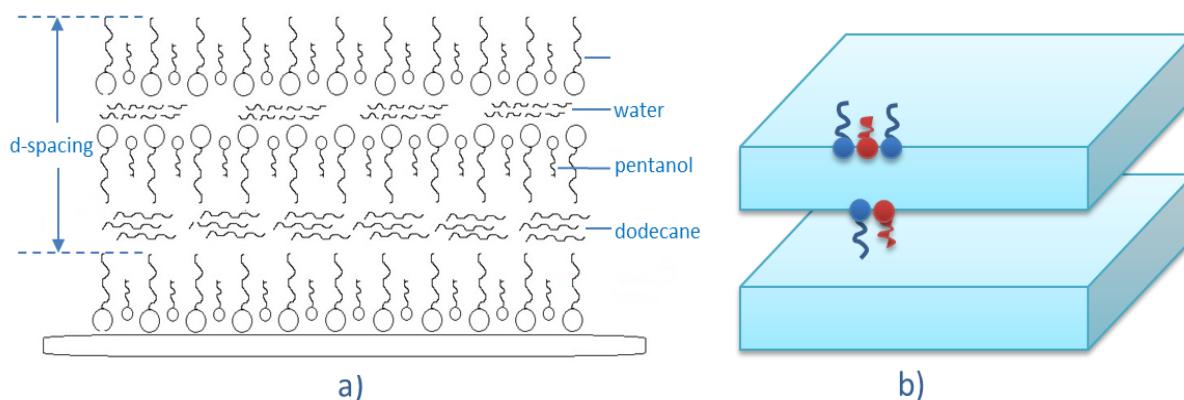


Figure-A12: a) The molecular structure of lamellar phase of Water-Pentanol-Dodecane-SDS system on carrying glass; b) Perfect lamellar phase with one dimensional positional ordered structure. The d-spacing is related to the concentration of solvent which is dodecane in this case.

Considering the ideal situation, there is no defect in this lamellar phase. The simplest circumstance is that the director is perpendicular to the layer surface and forms a perfect membrane structure as presented in Figure-A12 b). If we put the material without defect between analyzer and polarizer, and the membranes are parallel to the polarizers, then all the directors will also be perpendicular to both of the polarizers, so no light will come through the second polarizer.

3-2 Defects in the Lamellar Phase

In a real sample of liquid crystal, defects are often present where the director does not always point in the same direction from place to place. There are locations where the director changes its direction abruptly, and this phenomenon is referred to defects in liquid crystals [10]. Two main classes of defects, line defects and point defects, exist in Nematic liquid crystals. The line defect is named 'disclination' which indicates 'discontinuity' in the 'inclination' of the molecules [6].

The defects occurring in the lamellar phase are different from the Nematic liquid crystals due to its layered structure. Elementary defects are dislocations that contain two basic types, edge dislocation and screw dislocation [7]. The edge dislocation is more common in lyotropic lamellar systems, and it happens at the location where a membrane layer suddenly stops, as presented in Figure-A13.

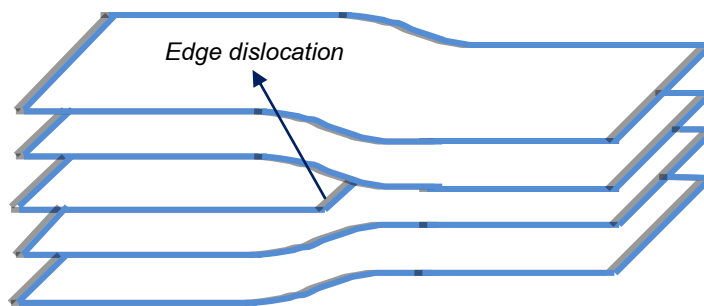


Figure-A13: An edge dislocation defect in the lamellar phase.

If a lamellar phase is observed between two crossed polarizers in an optical microscope, and the polarizers are oriented in the x and y direction respectively, then for a dislocation defect whose edge is oriented along the y direction (as pictured in Figure-A14), no light will emerge from the

second polarizer and we can only see darkness under a microscope. However, the defect edge can be easily observed if the material is rotated, because the director is no longer perpendicular to the polarizers. This is used to identify the orientation of the defect.

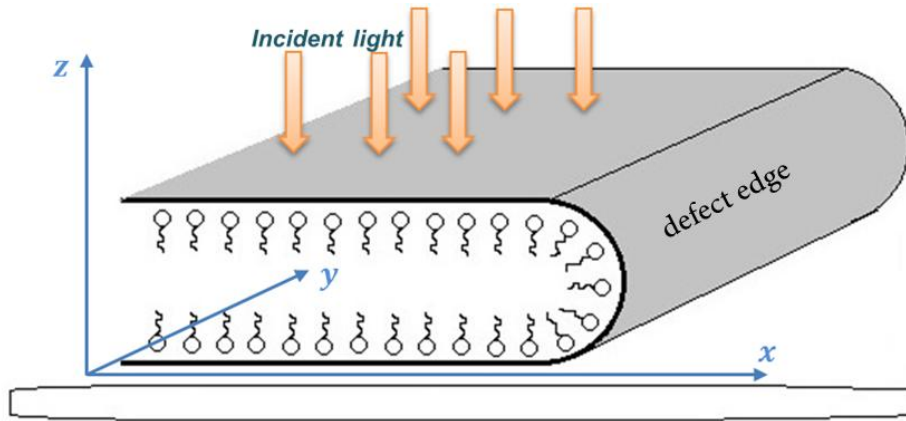


Figure-A14: Molecular structure of the edge dislocation in the lamellar phase. The defect surface is simply along the y direction, and the axes of two polarizers are pointing in the x and y directions, respectively.

Nevertheless, in this particular lamellar phase material, the edge dislocation defects are not straight and appear to be undulate as can be seen in Figure-A15 [20].

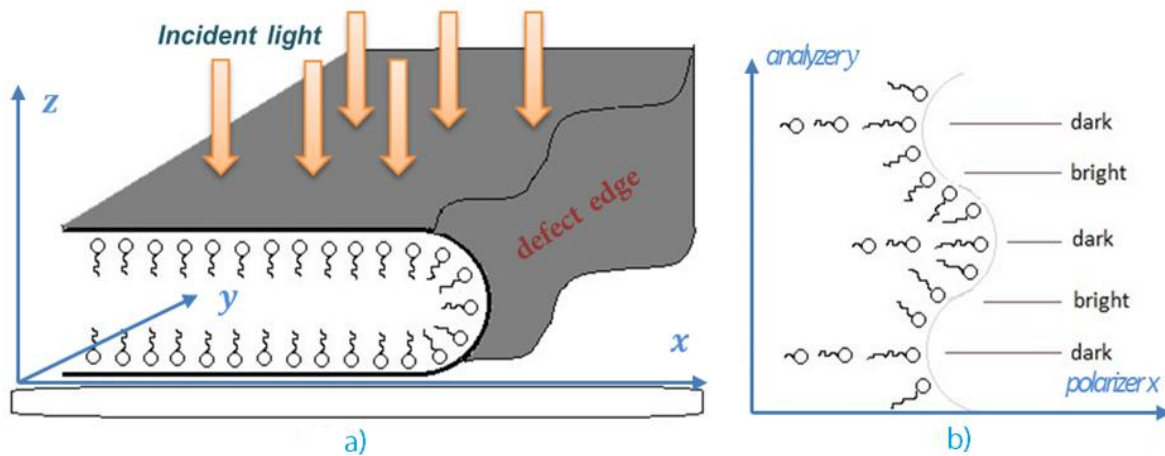


Figure-A15: a) A general defect in the lamellar phase with an unstraight and curved defect surface. b) Molecular visual observation from the top. The x and y directions are the axes of polarizer and analyzer, respectively.

Because the molecular chain's direction can represent the director, several situations will occur between the chains' directions and the polarizers' polarizations:

- 1) If the chain direction coincides with either of the polarizer, no light will transmit.
- 2) If the chain direction has a non-zero angle with the polarizers, some light will transmit.
- 3) If the chain direction has a 45 degree angle with both polarizers, the maximum light can transmit, and it is the maximum bright spot in the field of view.

Therefore, along the defect surface, we can get an alternative dark-bright pattern. However, it does not have a certain shape and the darkness and brightness are transmitting gently, as shown in Figure-A16.



Figure-A16: A few dislocations in lamellar phase are observed between two crossed polarizers under an optical microscope. The dimension of the image is about 0.22mmx0.22mm.

3-3 Multi-lamellar Vesicle (MLV)

The Multi-lamellar vesicle (MLV) is called 'onion' because of its onion-like structure, where bilayers which are made of surfactants are arranged in a concentric manner, as presented in Figure-A17.

Observed between crossed polarizer under a microscope, the multi-lamellar vesicle has a fancy appearance as shown in Figure-A18.

It is found that MLVs can be produced from a lyotropic lamellar phase by applying a certain shear rate, as well as by some other methods such as electrode method [15] and dry liquid hydration [8]. As discovered by Roux and co-workers, the characteristic size of the spherical particles has a linear relation to the inverse of the square root of the shear rate, $1/\sqrt{\dot{\gamma}}$ [5].

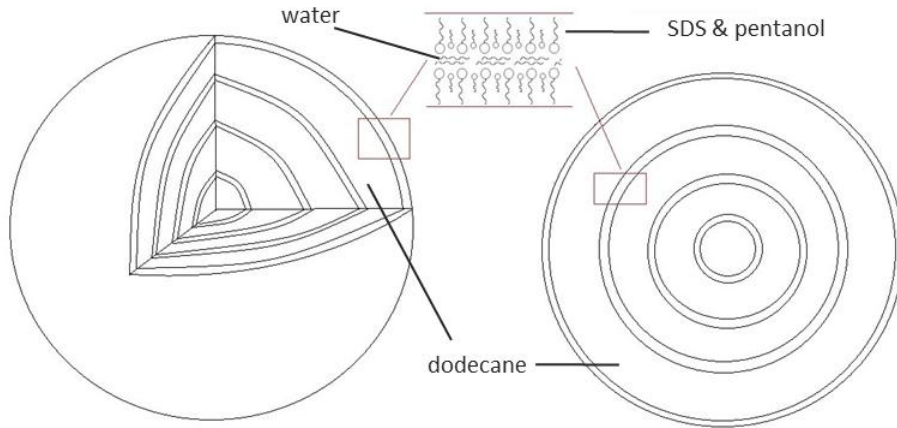


Figure-A17: Molecular structure of a multi-lamellar vesicle in a lyotropic solution. It is different from vesicles that are only one bilayer molecularly constructed.

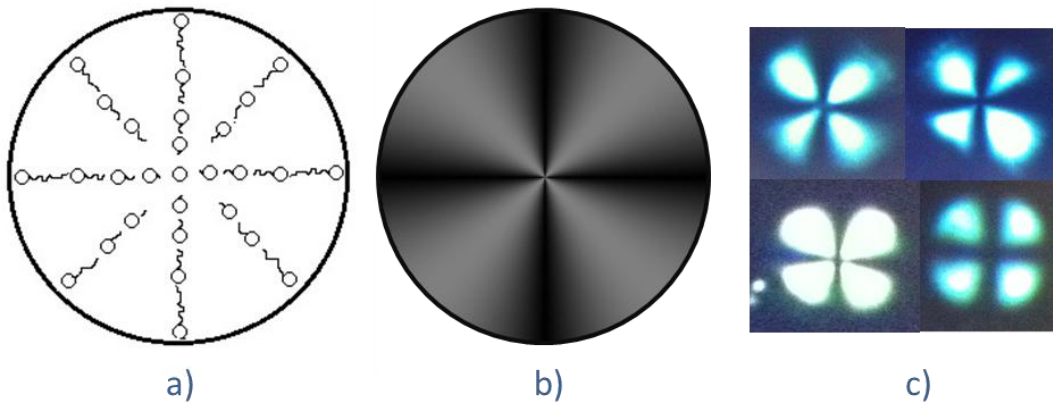


Figure-A18: a) Molecular structure for the cross section of one multi-lamellar vesicle observed from the top. b) Simulation observation of multi-lamellar vesicle between two crossed polarizers. c) Real patterns for multi-lamellar vesicles observed under microscope (they are not in the same scale and size).

3-4 Orientation States of Lamellar Phase under Shear

The Water-Pentanol-Dodecane-SDS lyotropic system has been extensively studied in the past, for a lamellar phase with various ratios of components, it was shown that the orientation and the structure of the material are strongly influenced by shear.

Roux and his group have done magnificent work on this special lamellar phase, and three different states of orientation as a function of shear rate and d-spacing have been well studied. This is summarized in Figure-A19 [9].

State I: happens at very low shear rates. Membranes are oriented in the shear plane, and a lot of defects are in the shear flow direction.

State II: appears at medium shear rates. The intermediate state shows that mono-disperse multi-lamellar vesicles are formed from membrane layers, and the size is well controlled by the shear rate.

State III: occurs at high shear rates. The membranes are basically pointing in the direction of shearing, and no defects in the flow direction are observed.

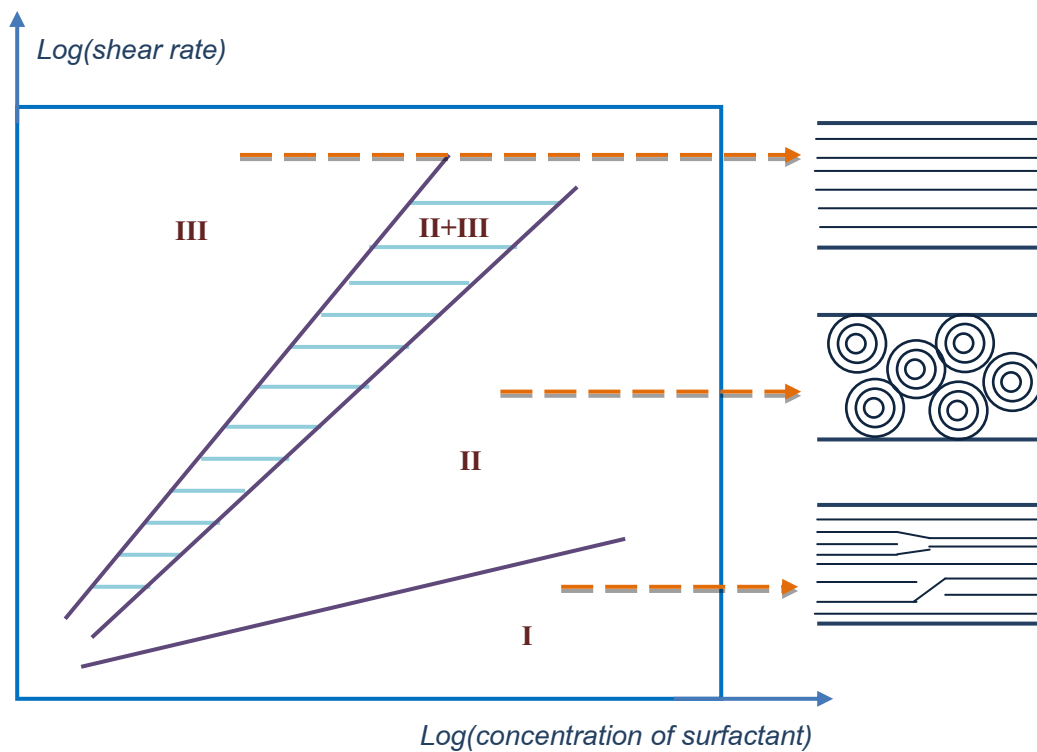


Figure-A19: Functional representation of orientation phase diagram for the Water-Pentanol-Dodecane-SDS lamellar system under shear [Derived from Diat O., Roux D., J. Phys. II France 3, 1431 (1993)], where detailed information and data can be obtained]. The y-axis represents the applied shear rate and the x-axis represents the concentration percentage of Water and SDS. This is a logarithmic scale of the orientation states versus concentration and shear rate.

The transition among these several orientation states can be continuous or discontinuous. For example, from State II to State III, there is a region where both states can coexist.

In addition, the multi-lamellar vesicle state can remain stable even after the shear stops.

Therefore, in some specific ways, for medical or research purpose, shear technology can be used to encapsulate drugs in well-defined multi-lamellar vesicles [9].

II. INSTRUMENT AND PROGRAM

1. Shear Machine

Based on the idea of Couette shear flow between two co-rotational disks, we are able to design a shear machine to observe the evolution of lamellar phase under different shear rates through a custom built polarizing microscope. AutoCAD is powerful software to help us design the shear machine and preview its functions.

1-1 AutoCAD Design of Shear Machine

The AutoCAD design is shown in Figure-B1, with the following description of each part:

Part 1: The outer frame, made of aluminum, is used to support the whole shear machine. There are two pieces, the upper piece and lower piece of the frame, and they are initially separated but can be joined together by screws. Also, we can control the distance between the two pieces by adding metal shims at the edges. Based on the shims which have various thicknesses (such as 0.13 millimeter and 0.25 millimeter), we can get different sizes of spacing between the two pieces of frames as well as the two pieces of disks. It was made in the machine shop located in the Department of Physics and Astronomy at the University of Waterloo.

Part 2: Two pieces of very flat round glass with a diameter of 125 millimeters and thickness of 6 millimeters were bought from Edmund Optics. The part number is A45-685. Each glass and each shaft are perfectly centered and were glued together in the machine shop. The shafts are fitted on the frames using bearings. The two pieces of glass are flat, transparent, and are set to be parallel to each other with minor tolerance. There is also a rim which is higher than the edge of the lower disk to prevent the fluid from spinning out while being sheared between the two disks. The distance between the two disks can be adjusted by changing the shims between the two pieces of frame.

Part 3: The two servo motors' model is Light Industrial Servo Motor LIS234-F-0804 with a NEMA23 standard frame size. They are controlled through a controller which is connected to a computer to allow for a smooth motion from 60 RPM to 4000RPM. By sending commands to

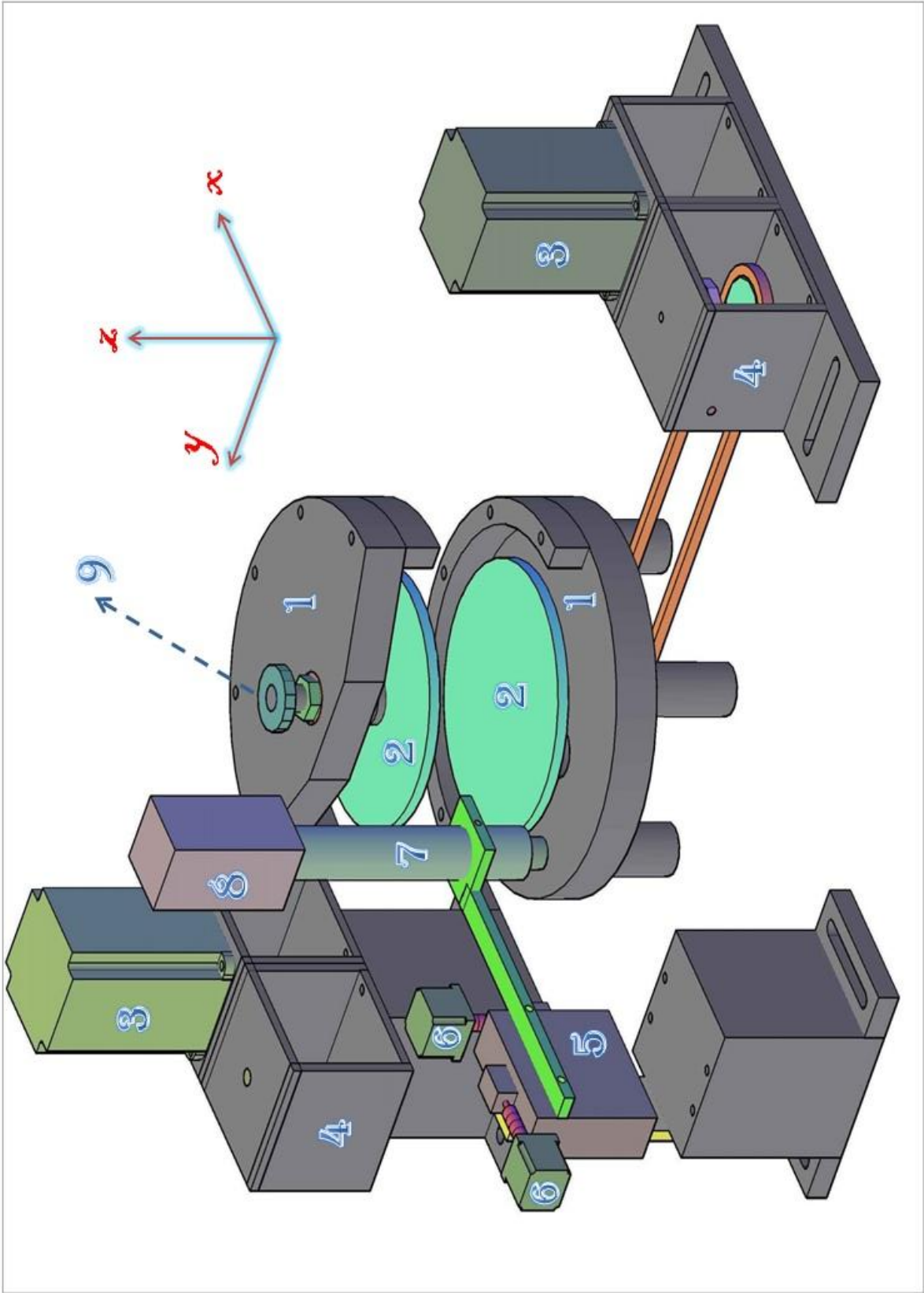


Figure –B1: AutoCAD design for the shear machine between two co-rotational disks. Some parts are not shown on the drawing, and the actual instrument may have minor difference from the CAD design.

the motors, we can change the speed immediately.

Part 4: The home made gear boxes or speed reducers were made to get a very low speed from the motors and connect to the shaft of the disks. Each gear box is made of two worm screws, two worm gears and shafts inside of two 3'' x 3'' cubes. The structure of the gear box is shown in Figure-B2; part 1) and 3) are worm screws and part 2) and 4) are the corresponding gears with the ratio of the gear to worm screw being 40:1. Part 1) is connected to the servo motor, and part 5) is another pulley associated with part 6) – the belt is connected to the disk. We can get a speed reduction of 1600:1 because of the two pairs of worm screws and worm gears. The reason we did this was to get a very low shear rate in steady motion without jerking so that the microscope can observe the lamellar phase in motion very clearly.

Part 5: The translation stage with two axes is holding the microscope, and one of the stages can move in the horizontal direction (or x axis) while the other can move in the vertical direction (or z axis). By moving the two stages, we can control the microscope to be in focus and in radius direction to get different distance to the center of the glass disks.

Part 6: Two stepper motors (model No. VEXTA C6944-9012) are linked to each stage separately and can be controlled by the computer through a stepper motor controller. Since the amount of displacement that the layers can move is limited to a maximum of 15 millimeter, we have two mechanical limits that the stepper motor can't exceed when moving to follow the particles in the shear cell.

Part 7: A homemade microscope with its objective lens and tube assembly is located here. To observe the multi-lamellar vesicles with sizes of only a few micrometers, we chose some objectives with a high magnification, long working distance and proper depth of focus. The objectives we choose to use are Nikon M Plan 10 and the Mitutoyo M Plan Apo 20 with infinity correction. In addition, there is a polarizer in the middle of the tube, and another linear polarizer is placed just after the light source. Two linear polarizers have axes crossed so that we can see the birefringence property of the lamellar phase. The optical light path will be discussed later.

Part 8: A CCD camera connected to the computer is used to capture the images from the microscope. The first camera model is the Sony XC-75 which gives us a 640x480 pixel resolution image, and the second camera model is the Qimaging Retiga EXi Fast 1394 which gives us a 1392x1040 pixel resolution image.

Part 9: There are two pulleys sitting on the shafts which are attached to the disks. Depending on the size of the pulley on the shaft and the pulley in the gear box, we can have more options for getting the total speed ratio of the motor speed to the disk speed. For example, to get a ratio of 1000:1, we use a 20 tooth pulley on the shaft of disk, and a 32 tooth pulley in the gear box to get a speed increase ratio of 1.6:1, and thus, the total speed ratio becomes $\frac{1600}{1} \cdot \frac{1}{1.6} = 1000:1$.

Besides, the pulley in the gear box is at the same height with the pulley on the shaft so that the belt will give us a smooth motion.

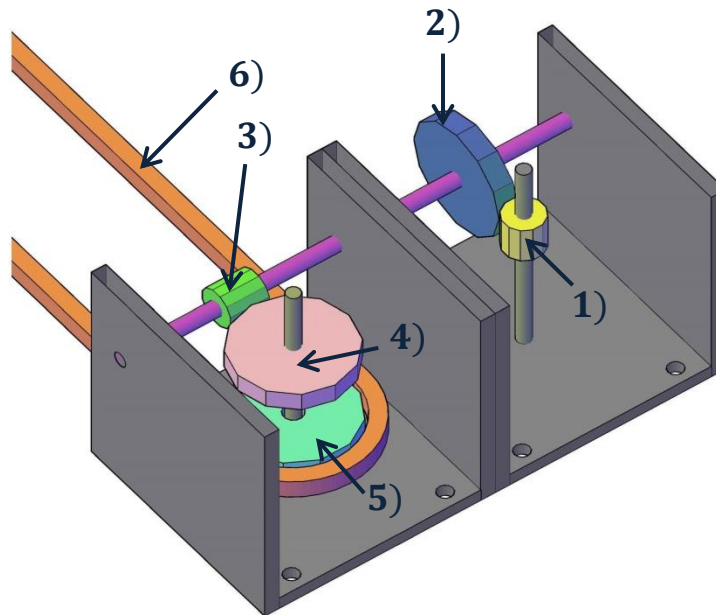


Figure-B2: The internal mechanics structure of the speed reducer for the servo motor. The drawing does not represent the actual appearance of the real objects. 1) and 3) are worm screws, 2) and 4) are the corresponding worm gears, the ratio is 40:1.

According to the AutoCAD design of the shear machine, we can know its basic function and how to use it from the beginning, and then make modifications based on what we need. There are also some other small mechanical parts on the shear machine that are not mentioned above,

such as the screws for holding shafts, the adapters between motors and shafts, the mounts for motors and gear boxes and so on, but they are also very important in building a perfect shear machine. The shear machine and motor speed reducer are fixed on a metal plate which is located on a vibration table, so all the components are at the right position and they can be connected to each other properly.

1-2 the Field of View

When doing an experiment, we need to put the rim around the lower disk and then add the fluid samples between the two parallel disks so that the fluid will not flow out of the disk. Then, we can put the shims with proper thickness between the lower frame and upper frame and screw them together tightly. After preparing the sample between the two disks, we can observe the sample under shear between two crossed polarizers with the microscope. The relationship between the image we get and the real situation is shown in Figure-B3.

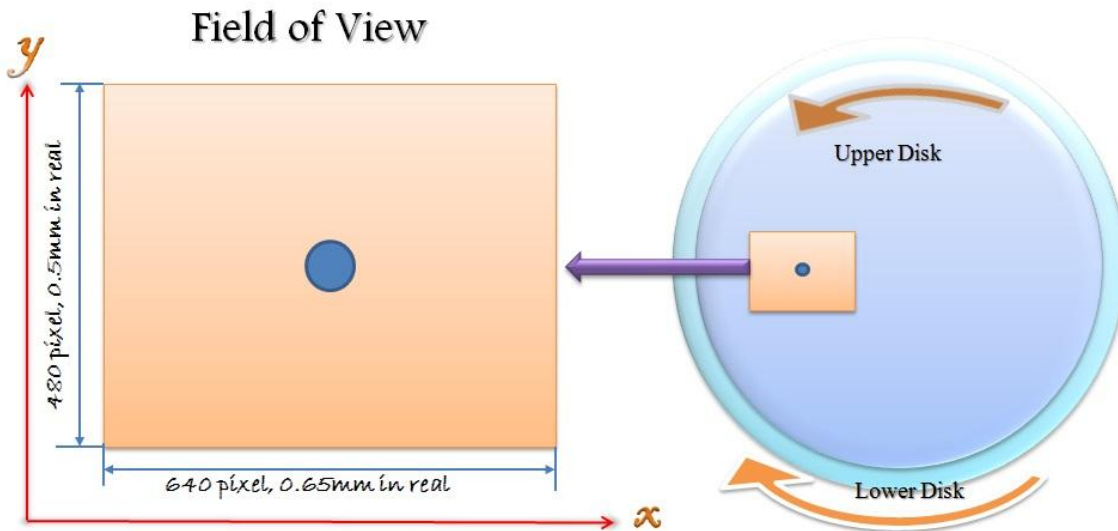


Figure-B3: The field of view for the microscope. The image that the CCD Camera (Sony XC-75) gives us has a resolution of 640x480 by using the objective Nikon M Plan 10. Horizontal direction \hat{x} is along the radius and pointing from the microscope to the center of the disk; vertical direction \hat{y} is perpendicular to \hat{x} direction and pointing upwards, along the surface of the disk.

The upper disk and lower disk are the same size. The microscope gets the top view for an area of only about 0.65x0.5mm. Observed from the top view, the upper disk is rotating in a counter-

clockwise direction and the lower disk is rotating in a clockwise direction. Because the field of view is so small, we can say that the upper disk is moving in $-\hat{y}$ direction, and the lower disk has a velocity in $+\hat{y}$ direction, so the motion in \hat{y} direction motion is given by the velocities of both disks. Also, the microscope can move in the direction along the radius, which is the \hat{x} direction.

Considering a particle in the field of view, we need it to always be in the center area of the field of view so that it can be observed well. Therefore, we need to adjust the speed of the disks and the position of the microscope to keep it in the center area if the particle moves out of the center area. There are two situations for the particle if it is not in the proper position: drift in \hat{y} direction, and drift in \hat{x} direction, which are demonstrated in Figure-B4.

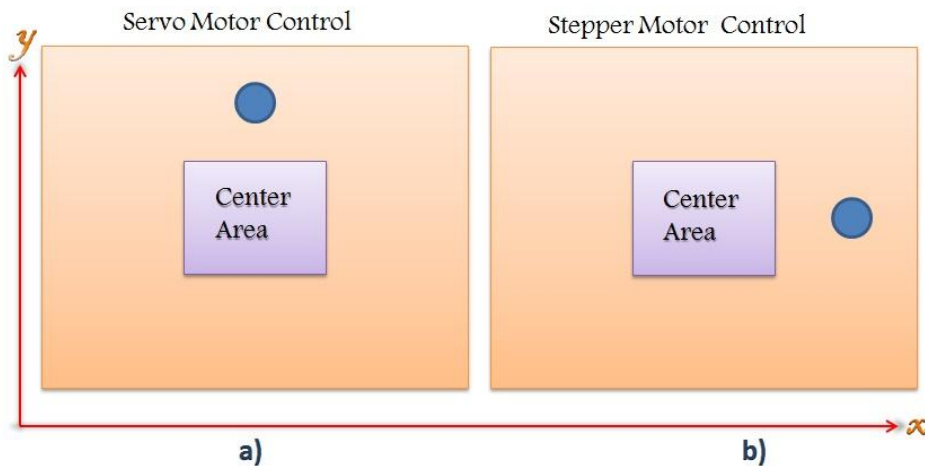


Figure-B4: The relationship between the position of particle and the control of the Servo motor or Stepper motor. a) Particle is out of the center area in \hat{y} direction can be re-centered by Servo motor control; b) Particle is out of the center area in \hat{x} direction can be re-centered by Stepper motor control.

For example, if the particle moves to the top of the center area, we can bring it back if we increase the speed of the servo motor which is connected to the upper disk, since the upper disk has a velocity in $-\hat{y}$ direction. The relative speed for the particle to the ground is increased in $-\hat{y}$ direction, and it will move down back to the center. For the situation that the particle is off to the right or left, we can control the horizontal stepper motor which moves forward and backward to produce the same amount of position offset. By this approach, we are actually moving the position of the microscope and changing the area of field of view. The reason why

we change the position of the microscope is that we cannot control the particle's motion in the radial direction.

1-3 Shear Rate Derivation

According to the design of the shear machine, we can calculate the shear rate between the disks in terms of the speed of the servo motors, as follows,

For each servo motor, suppose the angular speed is F (*revolution/min*);

the gap between the two disks is d (*mm*);

the gear box ratio is $\alpha: 1$;

the distance from the view to the center of the disk is R (*mm*).

For each disk, the angular speed is

$$\omega = \frac{F}{\alpha} \text{ (revolution/min)} = \frac{F}{60 \cdot \alpha} \text{ (revolution/sec)} = \frac{2\pi F}{60 \cdot \alpha} \text{ (radian/sec)}$$

At the view point, the linear speed is,

$$v = \omega \cdot R = \frac{2\pi F \cdot R}{60 \cdot \alpha} \text{ (mm/s)}$$

Since the two disks are moving at the same angular speed but in opposite directions, the shear rate becomes

$$\dot{\gamma} = \frac{v_1 + v_2}{d} = \frac{2v}{d} = \frac{2}{d} \cdot \frac{2\pi F \cdot R}{60 \cdot \alpha} = \frac{\pi F \cdot R}{15\alpha \cdot d} \text{ s}^{-1}$$

In the shear rate formula, F, R, α, d are the adjustable variables. To have a smooth motion for the servo motor, F is in the range of 60 to 4000 (*revolution/min*); R can be any value between 30 to 45 (*mm*) so that the microscope can observe it. Based on the design, α is picked from 20, 1000, 1600, 2500; we use $\alpha = 1000$ in the experiment generally. Theoretically, d could be any value in *mm* scale depends on the shim we use; we use $d = 0.254 \text{ mm}$ to obtain a proper depth of focus plane and enough gap for the liquid to flow.

If we choose some typical values for the variables, $R = 40 \text{ mm}$, $\alpha = 1000$, $d = 0.254 \text{ mm}$, the

shear rate becomes,

$$\gamma = \frac{\pi F \cdot 40}{15 \cdot 1000 \cdot 0.254} = 0.033 F$$

Therefore, in this situation, since F is in the range of 60 to 4000 RPM, a shear rate can be obtained as low as 2 s^{-1} , which is slow enough to observe the motion under the microscope, and as high as 130 s^{-1} . Besides, other variables can also be changed with the aim of getting a lower and higher shear rate.

1-4 Actual Equipment

Based on the AutoCAD design, we have the practical equipment which is shown in Figure-B5 and Figure-B6. There are some minor modifications from the original design.



Figure-B5: Bird's eye view of the whole equipment for the shear machine and the controllers by eye.

In Figure-B5, a) is the controller for the servo motors which has a PID control to give a better feedback from the motors and aid in minimization of errors; b) is the image processor which receives images from the camera and does some processing such as adjustment of brightness, contrast, subtraction of background and so on, to obtain better image quality; c) is a VCR that records the video from the image processor for data storage and later analysis; d) is a screen for watching the live video, whose output is connected to the computer; e) is the stepper motor

control; f) is the power supply and controller for the light source; g) is a vibration isolation table which reduces noise and vibration from the background. The servo motor controller and stepper motor controller are connected to the computer and commanded through the LabView program.

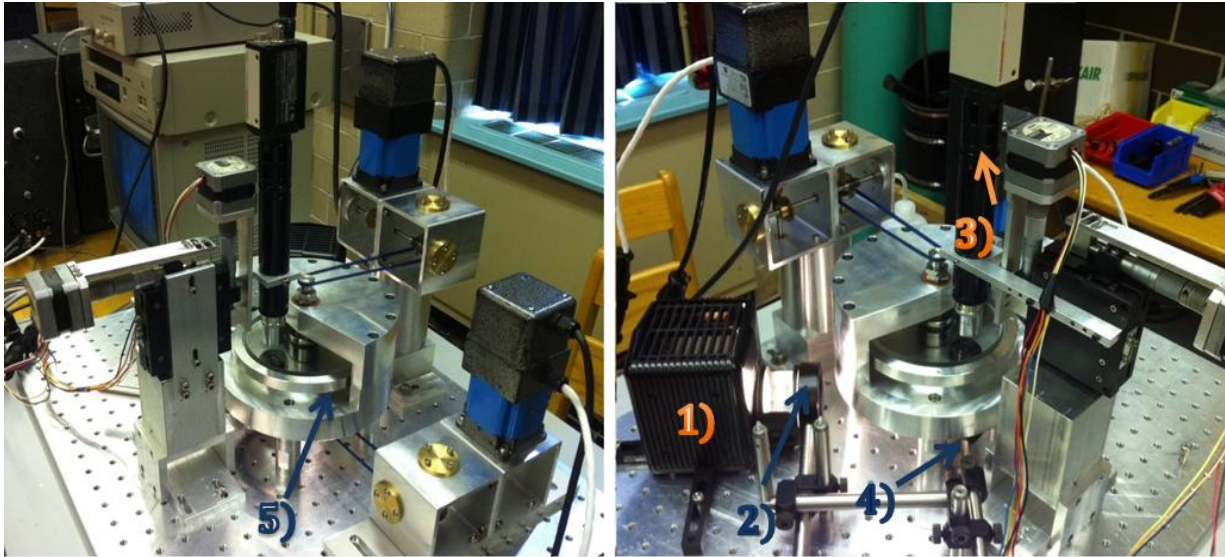


Figure-B6: The actual shear machine we have for the experiments. Some modifications have been made to make it perform better from the AutoCAD design.

Part 5) is the ring connected to the outside of the lower disk to prevent fluid splashing out; part 1) is the light source which produces uniform parallel light with high intensity; part 2) is the polarizer; part 3) is the analyzer and part 4) is a mirror to reflect the light to the sample and microscope.

1-5 Simple Polarizing Microscopes

A simple polarizing microscope is built for observing the evolution of lamellar phase and the light path is drawn on Figure-B7. The polarizations of the two linear polarizers are perpendicular to each other. The glass diffuser is used to obtain a uniform parallel light from the light source while the condenser is used to focus light on the sample.

If the sample is put between these two crossed polarizers, we can observe the birefringence property of the fluid sample.

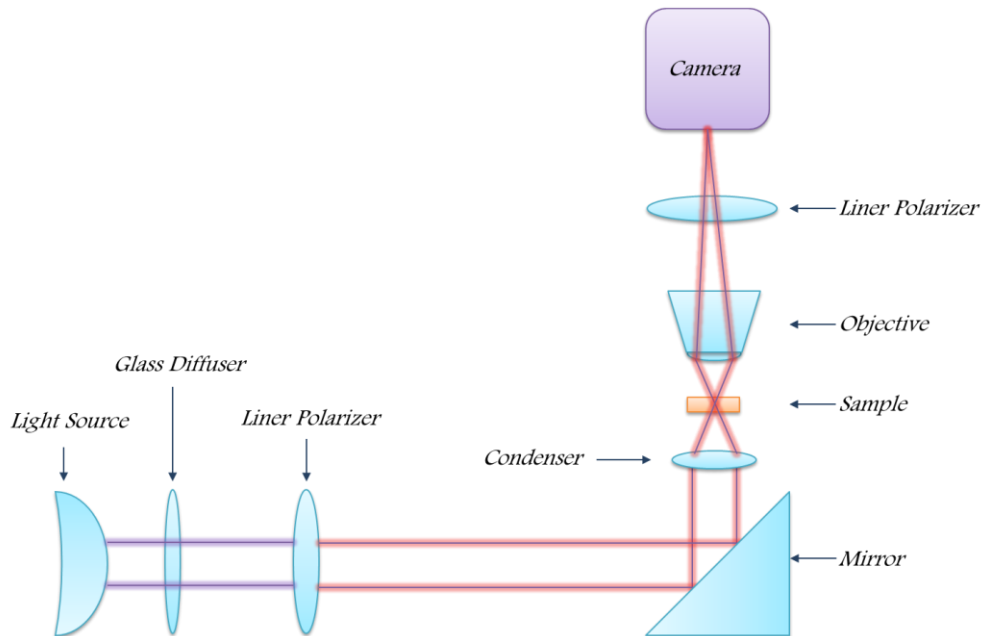


Figure-B7: The components and light path of the simple polarizing microscope from the shear machine. The two linear polarizers have their axes perpendicular to each other.

2. LabView Program Interface

2-1 Front Panel of the LabView Program

To control the motion of both servo motors and stepper motors, as well as video recording and image analysis, we use LabView which is very convenient for building a connection between the computer and instruments to achieve this goal. We need an interface that is very easy for us to perform and accomplish what we want to do. The graphical design of the interface is displayed in Figure-B8.

On the user interface, the 'ICI Image Control' is the live video coming from the camera. 'Image' is to get images from the video every few milliseconds, to detect particles in the fluid, and to get information of the detected particle such as position, area and so on, after image processing, enhancement and analysis. For a monochromatic image, the pixel value has a linear function with the level of brightness, and we have,

$$\begin{cases} \text{pixel value} = 0, & \text{total black} \\ \text{pixel value} = 255, & \text{total white} \end{cases}$$

Therefore, we can set a threshold value to separate the particles since the pixel value is different from the background, and we can continually set a pixel range to make the image have only two pixel values, 0 or 255. By doing this, we can have an image with black particles in a totally white background or white particles in a totally dark background.

'Setting' helps us identifying the particle that has a particular size, and getting rid of undesirable particles and unwanted impurities. It can also label the particles with numbers so we can know the density of particles in the field of view.

'Stepper Motor Control' allows us to control both stepper motors in one panel and also allows us to follow one particle automatically or manually.

'Servo Motor Control' gives us a direct view of both motors' statuses. We can start and stop both motors at the same time to make sure they are synchronous. Manual control is used to find the proper particles to follow, while automatic control is designed to follow particle without having to make individual operation. By inputting the value of the distance between two disks, and the radius to the center, the shear rate can be determined and seen on the panel.

2-2 Stepper Motor Following Particle

As was mentioned before, we can control the horizontal stepper motor to move the particle back to the center; the logic is shown in Appendix I:

Because the image has a width of 640 pixels and 0.65mm scale in \hat{x} direction, the distance from the particle to the center is $\Delta d = \Delta x \cdot \frac{0.65(mm)}{640} = (x(t) - 320) \cdot \frac{0.65(mm)}{640}$, according to the pixel coordinate.

For the manual control, we need to watch the video and make frequency operation on the image to make sure the particle would not move out of the field of view. Using manual control can avoid sending too many unnecessary commands to the motor, which allows us to follow the particle that the automatic control can not follow properly.

2-3 Servo Motor Following Particle

Speaking of following the particle in the flow direction, the idea is not the same with the stepper motor. The simple idea was explained before in Figure-B4 a).

For manual control, at the beginning of shearing, both the servo motors' speeds are set to the same value, for example, $200RPM$, and the value range for the slide control is -200 to 200 . During the shearing, by changing the value on the slide for a value of $\pm\Delta F$, the speed of the upper motor will change $\pm\Delta F$ too. The lower speed motor will change $\mp\Delta F$ at the same time as well. We use manual control to change the position of the steady layer with the aim of bringing some particle to the center area. Even though both motors' speeds are changed, the shear rate is kept to the original value all the time. For the situation where too many particles are in the field of view, we may not be able to follow one particular particle, but we can use manual control to lock onto one particle and keep it in the center such as playing a video game.

For automatic control, as shown in Figure-B9, suppose the upper disk has a velocity of v_1 , and lower disk has a velocity of v_2 . Initially, v_1 and v_2 have the same value of v_0 , so the velocity is zero at the center of the two disks. For an arbitrary time t_1 , one particle is at the position p , and after Δt time, it moves to position p' . If we want to keep the particle in the field of view, the layer where the particle is located should have zero velocity.

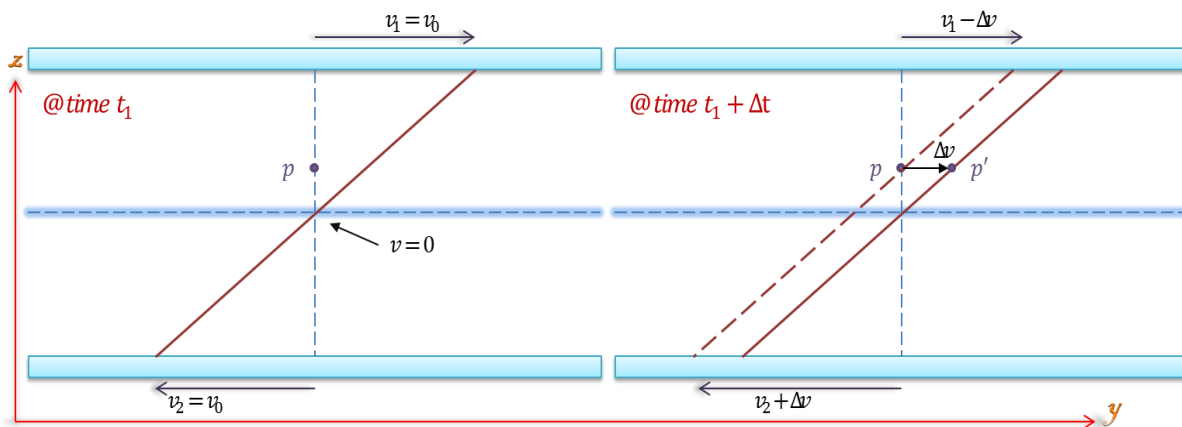


Figure-B9: a) The velocity profile at an arbitrary time t_1 for co-rotational disks, and a particle is at the position p . b) The velocity profile after Δt time and particle moves to position p' .

In a time interval of Δt , the particle moves a distance of Δy in y direction which can be obtained

through the image analysis, so the speed for the particle is $\Delta v = \frac{\Delta y}{\Delta t}$. Then the speed v_1 and v_2 need to be adjusted by Δv to stop the particle from moving.

$$\therefore \Delta v = \frac{\Delta y}{\Delta t}, \quad \omega = \frac{v}{r}$$

$$\therefore \Delta \omega = \frac{\Delta v}{r} = \frac{\Delta y}{\Delta t \cdot r}, \quad (\Delta y \text{ is in pixels; } r \text{ is in mm})$$

The image has a 640x480 resolution, and in shear flow direction, 480 pixels represent 0.5mm in distance.

$$\Delta \omega = \frac{\Delta y \text{ (pixel)}}{r \cdot \Delta t} \cdot \frac{0.5 \text{ (mm)}}{480 \text{ (pixel)}}$$

$$\Delta \omega = \frac{2\pi \Delta F}{60 \cdot \alpha} = \frac{\Delta y}{r \cdot \Delta t} \cdot \frac{0.5}{480}$$

$$\Rightarrow \Delta F = \frac{\Delta y \cdot 0.5}{480 \cdot r \cdot \Delta t} \cdot \frac{60\alpha}{2\pi} = \frac{\Delta y \cdot \alpha}{32\pi r \Delta t}$$

For $\alpha = 1000, r = 40\text{mm}$,

$$\Delta F \approx \frac{10 \cdot \Delta y}{\Delta t \cdot r}$$

Therefore, by applying a small adjustment of $\Delta F = \frac{10\Delta y}{\Delta t \cdot r}$ to the speed of the servo motors, we can make that layer have a relatively velocity of zero.

According to the above analysis, we have the flow chart attached as Appendix II.

Because the particle could move between different layers, when following the particle, the speeds of two servo motors are changing every cycle, depending on how far and how fast the particle moves. By doing this, we can lock the particle in the field of view to observe its evolution.

3. Modification of Instrument and Program

Based on the previous design and set-ups, we made some modifications on the instrument and

program to get images with higher quality and higher magnification. Firstly, the camera was changed to the Qimaging Retiga EXi Fast 1394 which has much higher resolution and higher shutter speed to capture particles in motion. Also, it gives us a 1392x1040 resolution image, and the exposure time and gain can be adjusted manually so we have the option of changing the grey scale for the image if the field of view changed. Secondly, the objective was changed to an infinity-corrected one with higher magnification and lower depth of focus to get a better illumination for the image and a better view for the structure of the lamellar phase under shear. The model for the objective is the Mitutoyo M Plan Apo 20 with 0.42 numerical aperture and 20mm working distance.

The LabView program was also modified; the front panel of the program is shown in Figure-B10.

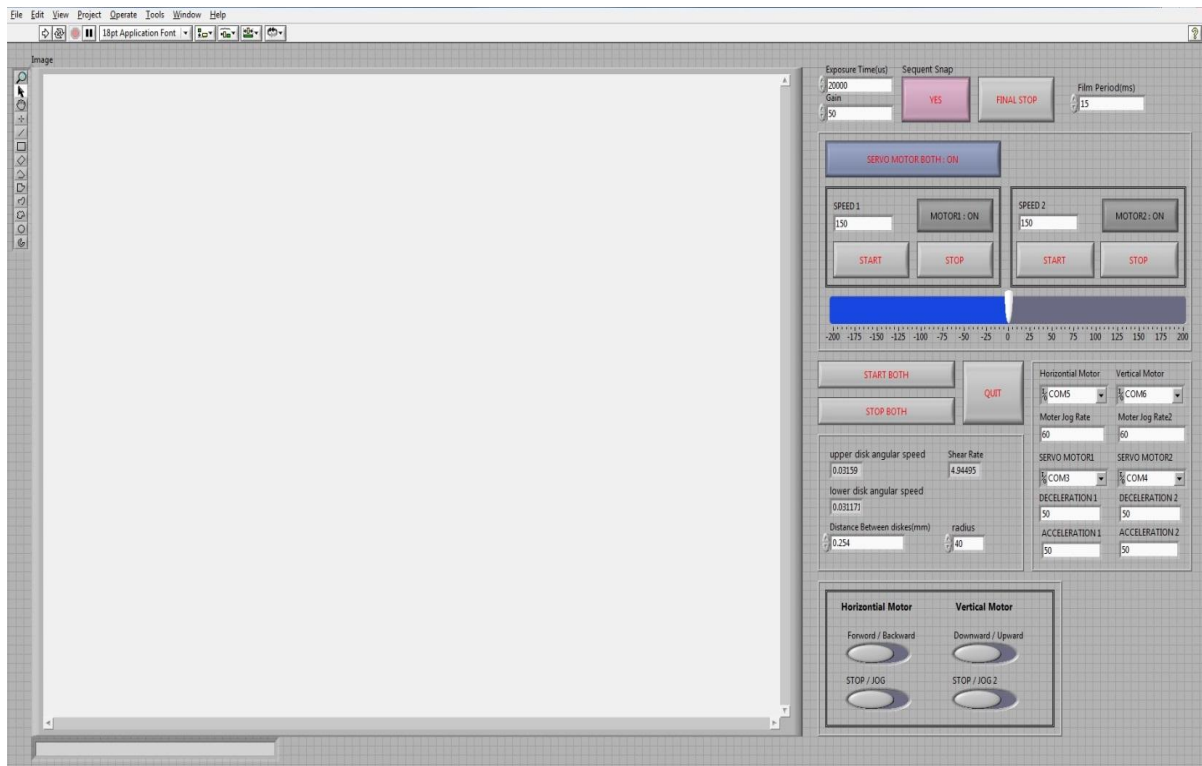


Figure-B10: The front panel of modified LabView Program. There are still sections for video, servo motor control, stepper motor control and image grabbing control.

The program is designed to grab images from the camera every few seconds. The servo motor control and stepper motor control parts are basically the same from the last program. A new

image grabbing control was added to control the exposure time, gain, and time interval for acquiring images. Therefore, we can store the images on a hard drive and analyze them over time.

4. Sample Preparation Procedure

The preparation of a lyotropic lamellar phase sample made by SDS, pentanol, dodecane and water is simple and easy.

Firstly, we need to choose the proper samples from the ternary phase diagram of Water-Pentanol-Dodecane-Water system to make sure they are lamellar phase. According to the previous work of Roux's group, we can make a series of lamellar phase solutions by mixing a dilution (91% dodecane + 9% pentanol) and a concentrated lamellar phase (31% dodecane + 18% pentanol + 51% SDS and water with ratio 1:1.55) [4].

Then, calculate the detailed composition of each component for all the samples we need from the above mixture. For example, we need 6.27% of SDS, 9.73% of water, 72.18% of dodecane, and 11.82% of pentanol to compose a lamellar phase SDS+Water at 16% concentration. We then calculate the mass of each component from the total mass of the sample that we want to prepare, and then put all the details into a table.

Use digital analytical balance to measure the accurate amount of each component and add into a glass bottle in the following order: SDS, dodecane, pentanol, and water. Seal the bottle and use vortex mixer and shaker to get a uniform mixture. Leave the samples for two days until all bubbles disappear; the samples are then ready to use.

5. Overall

The combination of the shear machine, motors, controllers, LabView interface and so on provides us with a whole system to track one single multi-lamellar vesicle, and to observe the

evolution of different orientation states of lamellar phase of SDS-Dodecane-Pentanol-Water solution under shear. One thing that needs to be mentioned is that the experiments were performed at room temperature. When shearing the fluid, the situation is not that simple and ideal; particles are either too crowded together or are not obvious from the background and thus, one single multi-lamellar vesicle cannot be easily identified or followed by the automatic control. However, we can always use manual control instead to achieve the purpose of one single multi-lamellar vesicle.

III. RESULTS

1. Sample Preparation

Based on the ternary phase diagram for the Water-Pentanol-Dodecane-SDS solution, we can make a series of samples from a very low concentration of surfactant to a very high concentration. The high concentration lyotropic lamellar phases will not transition to the MLV orientation state at low shear rates [4]. We aimed to observe the movement of a single MLV under microscope, so shearing a dilute sample at a lower rate is a good choice for us to achieve our aim.

Therefore, various samples at different concentrations, from 16% to 32% of SDS+Water, are prepared with the compositions shown in Table-D1.

Samples	(SDS+Water)%	SDS%	Water%	Dodecane%	Pentanol%
#0	12.00	4.70	7.29	76.90	11.12
#1	16.00	6.27	9.73	72.18	11.82
#2	18.00	7.06	10.94	69.82	12.18
#3	20.00	7.84	12.16	67.47	12.53
#4	22.00	8.63	13.37	65.12	12.88
#5	24.00	9.41	14.59	62.76	13.24
#6	26.00	10.20	15.80	60.41	13.59
#7	28.00	10.98	17.02	58.06	13.94
#8	30.00	11.76	18.24	55.71	14.29
#9	32.00	12.55	19.45	53.35	14.65

Table –D1: Prepared samples for the experiment according to the ternary phase diagram.

The ratio of SDS to Water remains constant at 1:1.55, and dodecane is taken as a solvent so the d-spacing between lamellae will increase if more dodecane is added. Among the above samples, in terms of (SDS+Water)% at 32% (sample #9) the smallest d-spacing occurs; while at 16% (sample #1) larger spacing between two molecular membranes occurs.

The d-spacing for the lamellar phases can be quickly determined by using x-ray diffraction, and the diffraction patterns for some samples are demonstrated in Figure-C1.

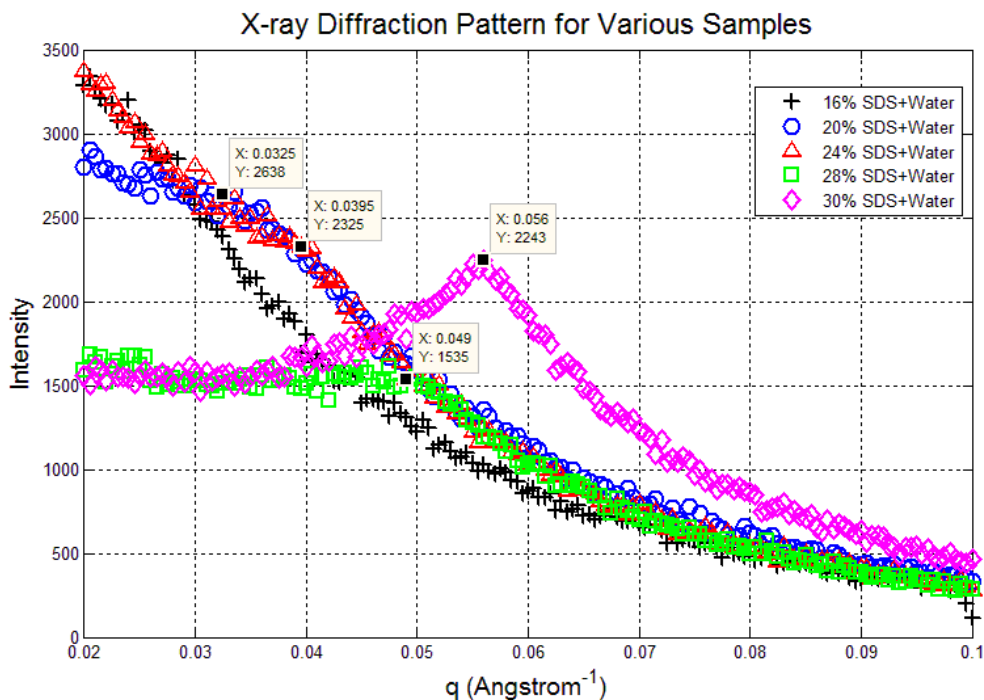


Figure-C1: X-ray diffraction patterns for samples with SDS+Water concentration of 16%, 20%, 24%, 28% and 32%. The X-ray diffraction method is used to detect the molecular structure of crystalline. If the crystal has a parallel membrane structure with a spacing of d , the x-ray diffraction pattern will give us an intensity peak at the scattering vector $q = \frac{1}{d}$, which can be obtained from Bragg's Law.

From the above diffraction pattern, we can obtain that the d -spacings for 20%, 24%, 28%, and 32% samples are about 38Å, 25Å, 20Å, and 18Å, respectively. The d -spacing for the 16% sample is not in the detectable range.

2. Following one Single MLV under Microscope

We want to observe the formation and evolution of one single multi-lamellar vesicle under shear flow directly using a polarizing microscope. The field of view of the constructed microscope is approximately half a millimeter. If the particle in the field of view is clear and easily distinguished, we can automatically follow the particle using the designed Labview program. However, it turns out that the size of the MLV is usually only a few micrometers and they are all over the field of view, so it is hard to keep track of one single MLV automatically. There are also some rare multi-lamellar vesicles of large size appearing when the lamellar phase

is under shear. These can be stabilized in the center area of the field of view manually and observed as time goes on.

2-1 MLV Observation by the Designed Equipment

As long as one good MLV appears under the microscope, we can manually control the speed of two servo motors and the position of the microscope to achieve the goal of following the particle as was discussed in Figure-B4. Below Figure-C2 shows one large MLV observed under polarizing microscope when a 12% sample is under shear rate $6.6s^{-1}$, and Figure-C3 demonstrates the appearance of the MLV versus time.

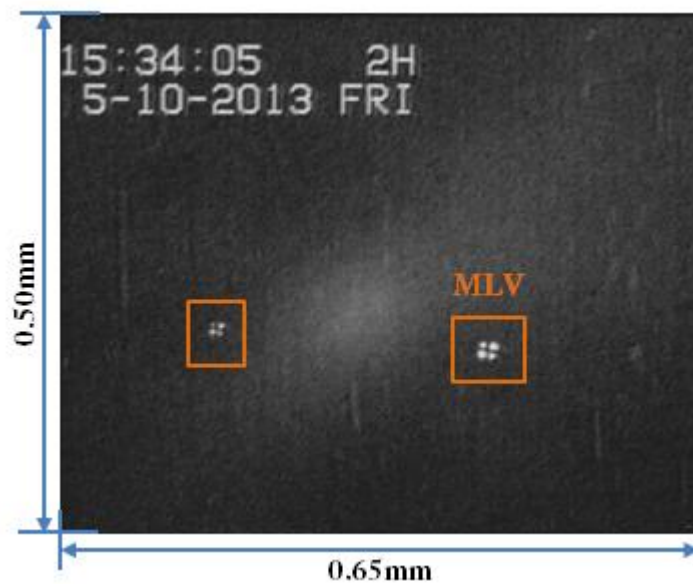


Figure-C2: One large MLV with size of about 30 micrometers as seen under microscope. Once it moves into the field of view, we can manually keep track of it.

There are also many MLVs with smaller sizes in the image, but they are moving fast and not in focus, so it is difficult for the camera with a low shutter speed to catch them in motion. The MLVs that are not at the stable layer will not be well monitored and shown in the image.

2-2 One MLV versus Time under shear

When the described MLV jumps into the field of view and is not moving rapidly, the speed of the two driving motors is adjusted to stop the MLV from moving in the shear direction in the image, and after that we can just focus on the MLV and record the video.

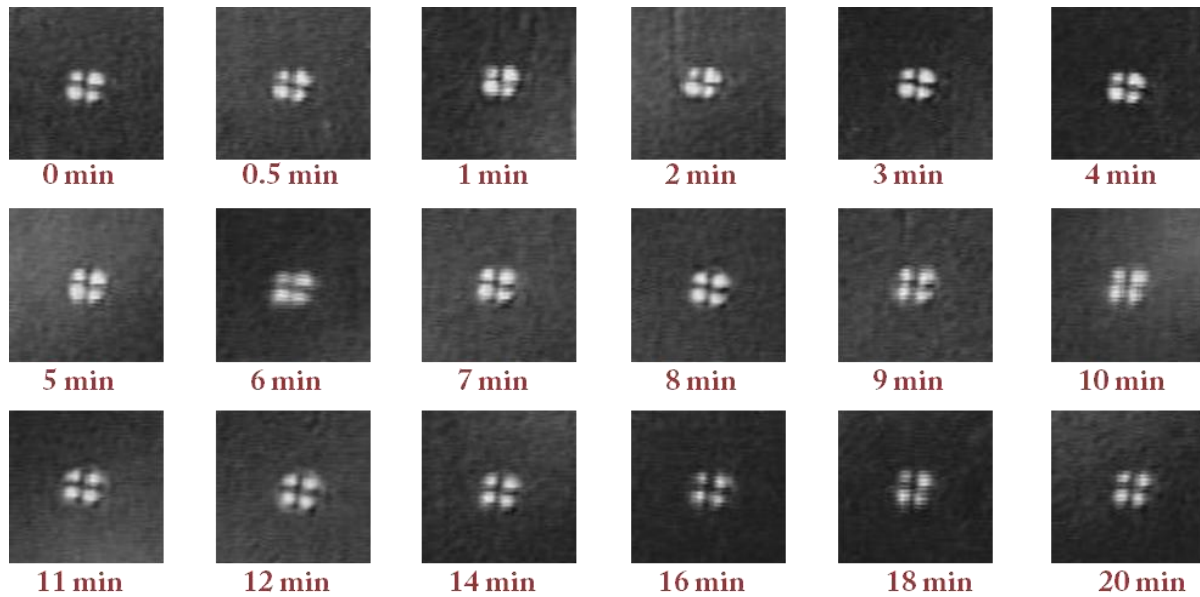


Figure-C3: A series of images for the same MLV at different times. They are grabbed from a recorded video that shows the entire process of following a MLV for 20 minutes.

By using the hardware equipment and a software program, a particle tracking system is built to either follow a particle manually or automatically. Because the position of the microscope is limited from 30mm to 45mm from the center of the disk, we were only able to track a single MLV for about 20 minutes. However, we can keep tracking the particle more than that as long as the microscope can reach it.

As observed from Figure-C3, in 20 minutes, the MLV basically remains the same size and shape. This is only one case, and there are more recorded videos obtained from the experiment, but no obvious change is found for the large MLVs that we followed. Several experiments have been performed but the results still could not tell us how the MLV is formed from the lamellar phase. On the other hand, we can determine how long it takes to go from the lamellar phase transition to the MLV orientation state after modifying the camera and program.

3. Lamellar Phase under Shear

3-1 Image Observations under Simple Polarization Microscope

After replacing the camera to one with a higher shutter speed and higher resolution, we can

acquire better images even at a higher shear rate. Then by gathering hundreds of images that are snapped every few seconds, we can observe the structural change from starting shear to the formation of the MLV orientation state. A sample with 24% SDS+Water is put between two disks with separation 0.25 millimeter under a shear rate of $5.0s^{-1}$; the images obtained at different times are shown in Figure-C4.

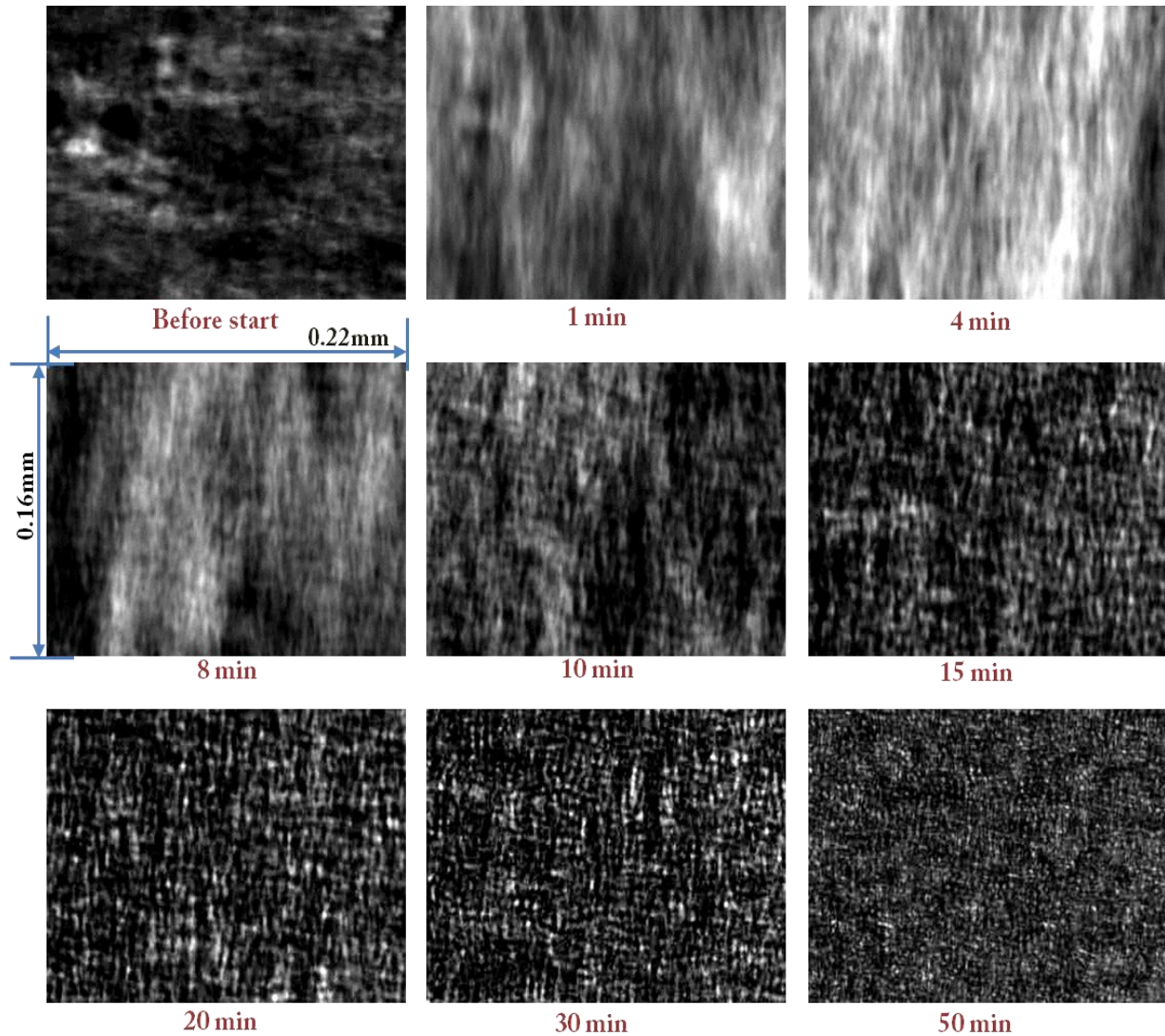


Figure-C4: Images obtained for a 24% lyotropic lamellar phase under shear rate $5.0s^{-1}$ at different time within an hour. These images are cropped from the original images with dimension 0.88×0.66 mm, and the brightness and contrast are adjusted to get a better view.

From the previous images, we can tell that the lamellar phase is changing with time. Firstly, the very obvious change is the brightness, and there is a time point when the average pixel value

reaches a maximum. Secondly, the structure or the orientation is changing. Because the sample between two disks is thick compared to the depth of focus of the objective, the image may not be sharp and clear. Consider the image at 50min, as shown in Figure-C5.

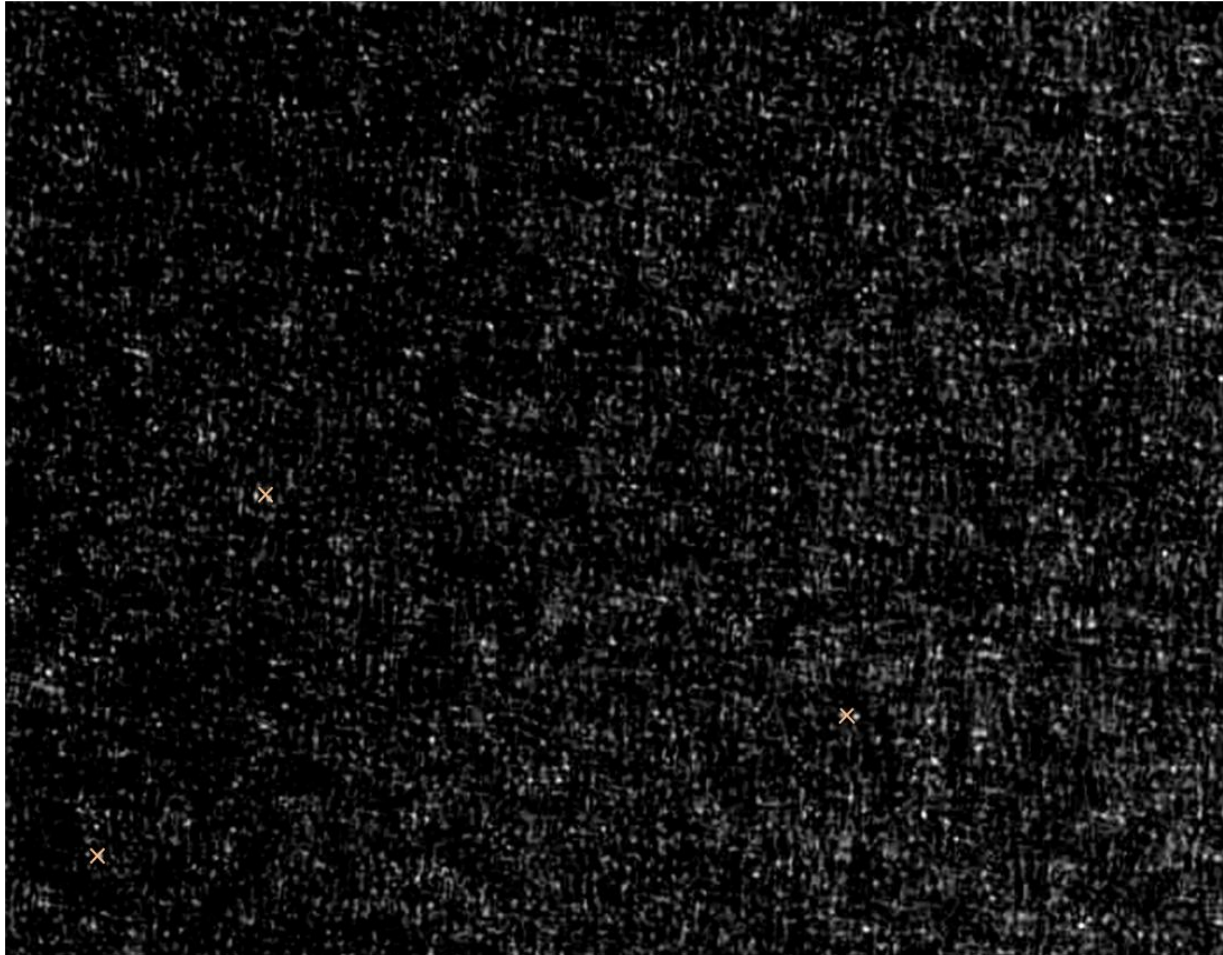


Figure-C5: The image is taken at time $t = 50$ min, with a dimension of $0.44\text{mm} \times 0.33\text{mm}$. The brightness and contrast is adjusted to have a better look on the structure.

In Figure-C5, we can see lots of small crossing patterns all over the image which are what MLVs look like under crossed polarizers as we discussed before. Because the MLVs are really small here, and some of them are not in focus, the patterns are not as good as we expected and it is not easy to get the average size of MLVs. In this case, the lamellar phase under shear rate 5.0s^{-1} will eventually change to MLV orientation state, and we can acquire the transition time from the series of images that are related to time.

Even though the change can be observed from the raw images, the position where the change

happened cannot be easily determined unless we find a proper way of analyzing the images.

3-2 Average Intensity Analysis

Since the brightness and intensity of the images is changing, the simplest method is to analyze the intensity change versus time. For each sample we have made, the shear rates we applied are $3.3s^{-1}$, $5.0s^{-1}$, $6.6s^{-1}$, $9.9s^{-1}$, $13.2s^{-1}$. The plot of average intensity of image versus time for 24% sample is drawn in Figure-C6.

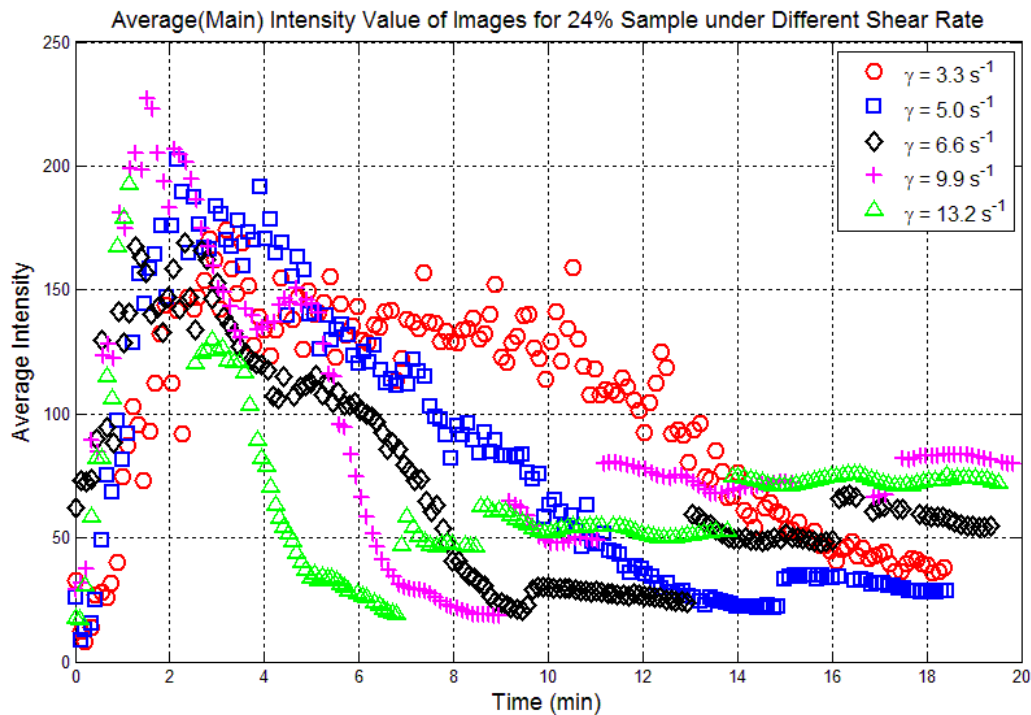


Figure-C6: Average Intensity of Images for 24% Sample at five increasing shear rate. The x-axis represents the real time. Data pass 20 minutes are not plotted so can see the peaks more clearly.

At the maximum intensity position, the defects in the lamellar phase reach a maximum and maximum brightness is observed under polarizing microscope because of the birefringence property. Roughly speaking from the above plot, the higher the shear rate, the faster the peak appears. The appearance of abrupt changes of the intensity (for example, the point at 7min under $13.2s^{-1}$ shear rate) is the consequence of the adjustment of exposure time or gain for the camera. However, the intensity plot of an image cannot represent the structure change of the lamellar phase, so the transition time cannot be derived from it.

3-3 Fourier Transform Analysis

The Fourier transformation of an image is used to transfer the image from the spatial domain to the frequency domain, or as we can say, from the grey scale distribution function to the frequency distribution function [22].

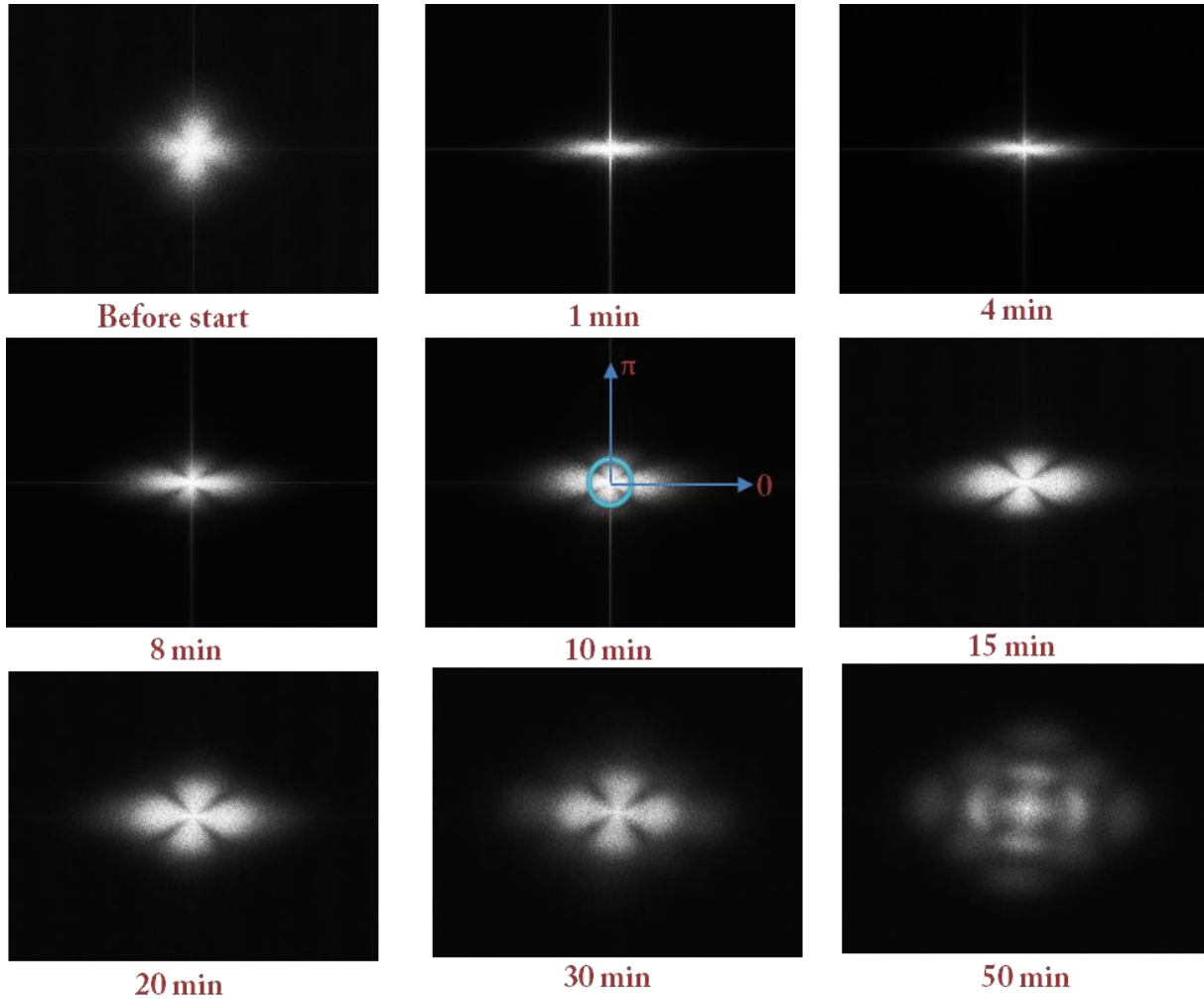


Figure-C7: Fourier transform images for the corresponding raw images in Figure-C4.

Therefore, if the orientation structures of the lamellar phase are not the same, then the Fourier transform images should also be different. By applying the Fourier transformation to all the images, we can analyze the change of frequency distribution with time, and then get the transition time. Figure-C7 represents the Fourier transform images for the corresponding raw images in Figure-C4.

In previous works on lyotropic lamellar phase under shear, light scattering [4] and neutron scattering [16] methods were used to explore the structure in the lamellar phase. The scattering patterns are typically shown in Fourier space [16], and they have some certain intensity distribution along a ring at the center. Besides, the Fourier transformation of an image will not be affected by the brightness of the raw image as long as the grey scale gradient remains the same. The brightness of the raw images can be influenced by the concentration of the surfactant and the exposure time of the camera. We also cannot tell the exact transition time from the raw images. Thus, taking the Fourier transformation of the raw images will give us a better and consistent view of the structure and the transition for all lamellar phases with various concentrations and should quantitative permit a description of the transition time. These are the reasons why we chose Fourier transform analysis for the raw images.

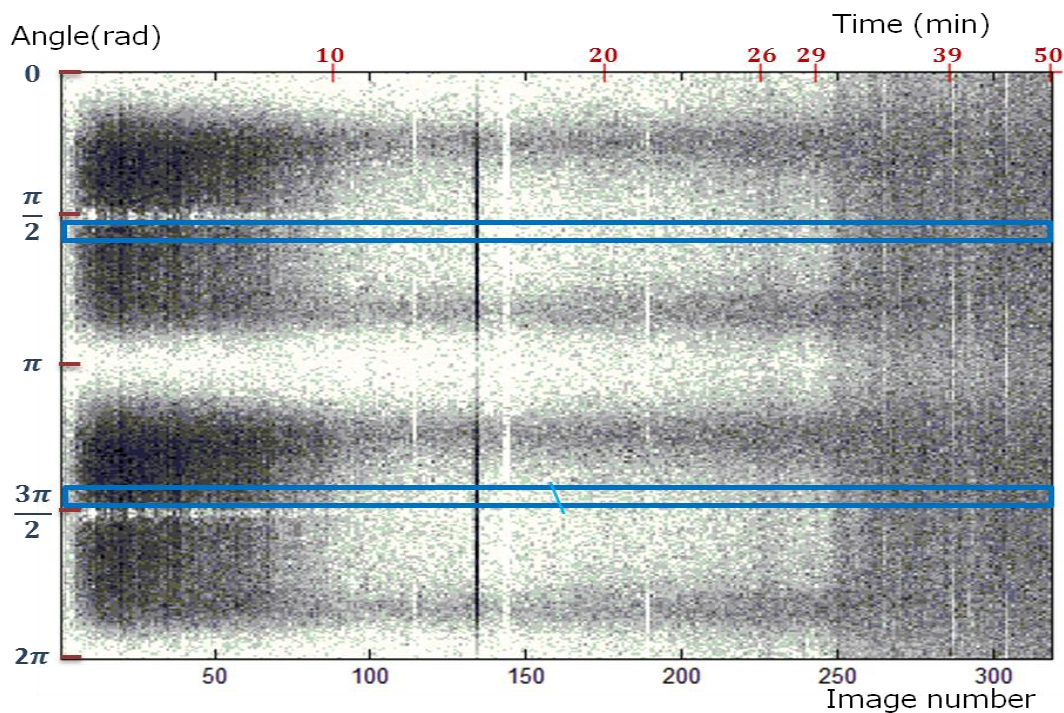


Figure-C8: Average pixel value along the same size circle as a function of azimuthal angle for all the Fourier transform images. The two rectangles which represent lines with certain width are used to draw the average intensity distribution according to the image number.

The Fourier transform images are much easier to analyze because the images in the frequency domain have particular intensity distributions in the center area. Then if we calculate the average pixel value along a circle, centered at the origin, as a function of azimuthal angle, which

is shown on the center image in Figure-C7 for hundreds of images, we will determine where the transition happens and how it changes. For hundreds of Fourier transform images, the plot of average intensity from angle 0 to 2π rad versus image number and time is shown in Figure-C8. As an image, the image number is along the x-axis while the intensity (given as a grayscale) is present at along the y-axis.

We stored each image according to the real date and time, so the image number is fundamentally chronological, but not linear in time. For example, as presented in the above figure, images are saved for every 7 seconds in the first 26 minutes, then 10 seconds between 26 to 29 minutes, then 14 seconds between 29 to 39 minutes, and then 20 seconds from 39 minute to the end. We can see that there are some white lines or dark lines, and these come from unwanted images which contain impurities. For later analysis, these images will be discarded in case that they affect our results. As long as we can get the relation between the transition point and correct image number, we can know the transition time.

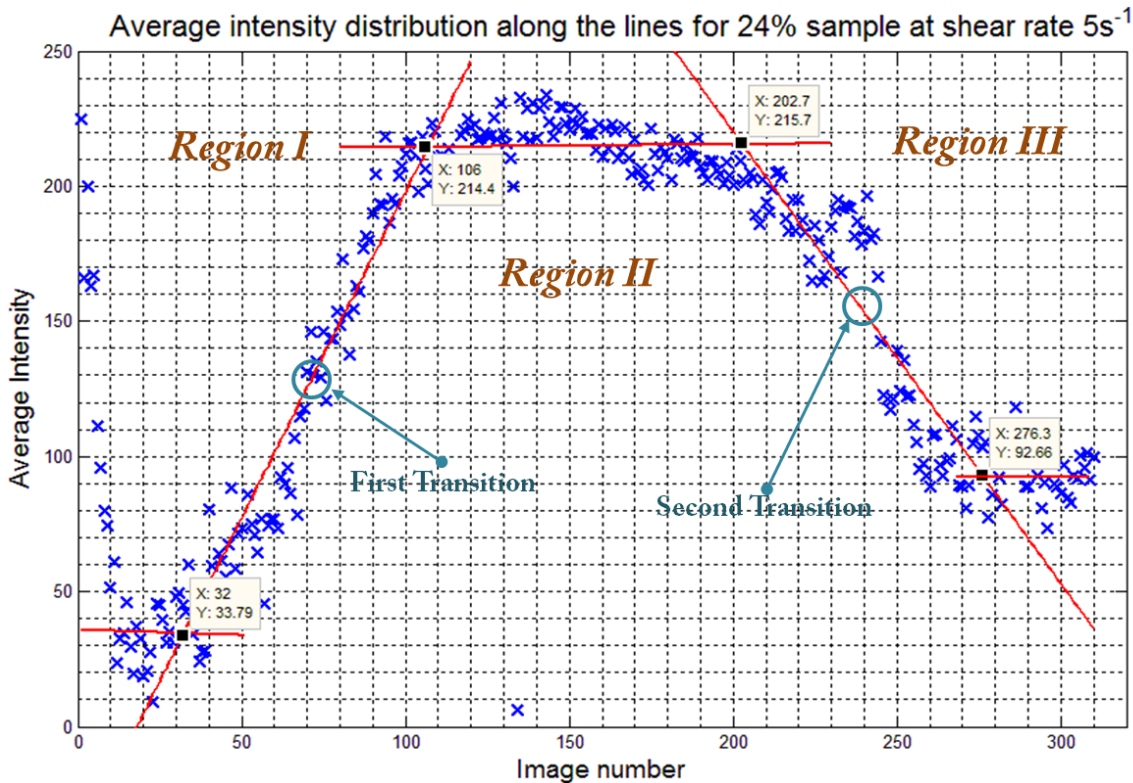


Figure-C9: Average intensity distribution along the lines of constant azimuthal angle versus image number for 24% sample at shear rate $5.0s^{-1}$. These are extracted at an angle of 0.57π and 1.47π radians, and are averaged over a width of 9 pixels for each line.

It is apparent that there are two transitions, and to get the transition time, a grey scale profile along wide lines is obtained, as shown in Figure-C9. The reason we use the ring and the lines with some width is to get the average intensity and to get more accurate values and results.

The process of the two transitions is slow and not sharp, so after acquiring the start and end transition points by using the intersection of two fitted straight lines, we can calculate the middle point as the relative transition point. For example, the two transition points here are image number 69 and 240, then we can get the transition times as 470 seconds and 1727 seconds after finding the real time according to the image numbers.

Two transitions give us three regions, in which typical images are shown in Figure-C10.

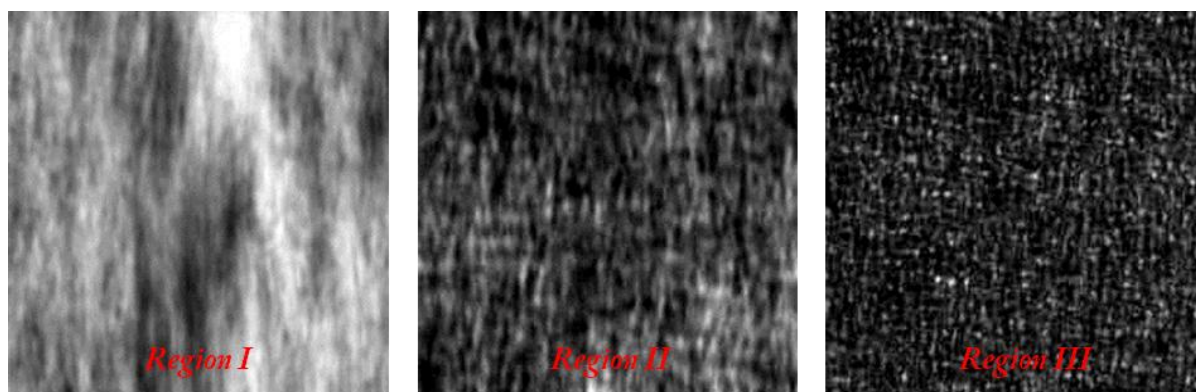


Figure-C10: Typical images represent the lamellar phase in three different regions. They are cropped from the original images to get a better view.

Region III is the final state after shearing for over 30 minutes, and this is the MLV structural state. *Region I* is the state where lots of defects are along the direction of shear flow. *Region II* is a mixture of *Region I* and *Region III*. *Region II* is an intermediate state for the lamellar phase transition from *Region I* to *Region III*.

For the 24% SDS+Water sample under different shear rates, the intensity distributions for the ring and the lines from Fourier transform images are shown in Figure-C11.

We can also obtain the average intensity distribution along the lines versus real time as shown in Figure-C12.

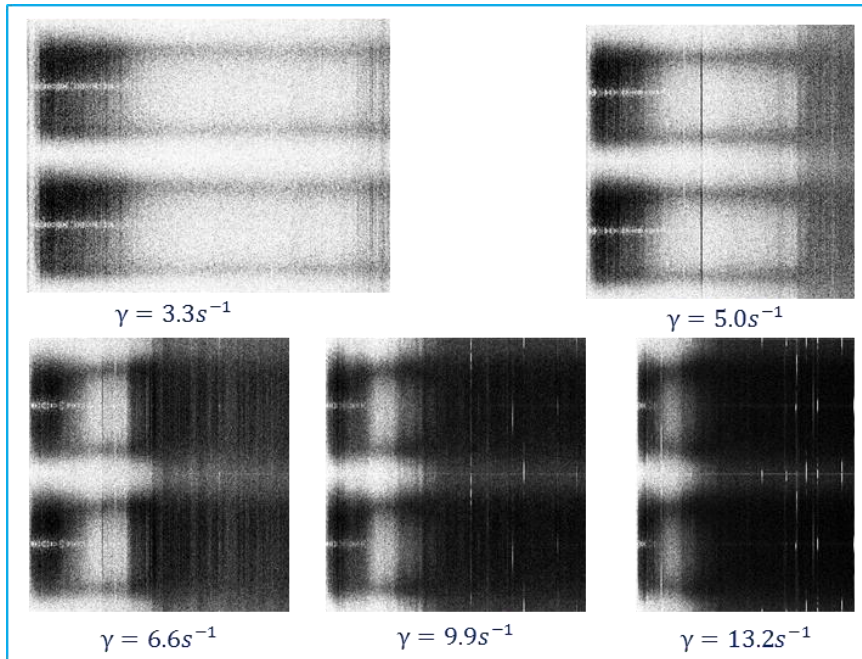


Figure-C11: The Average pixel value along the ring for all Fourier transform images for 24% sample at various shear rates.

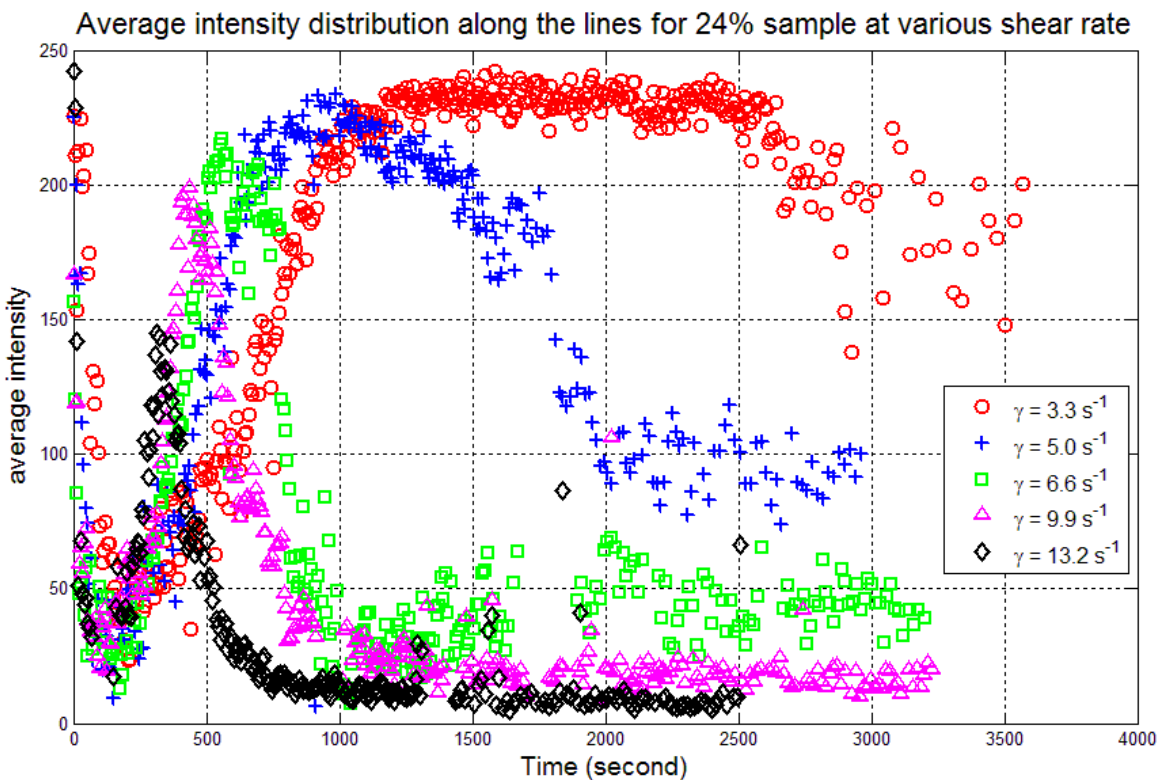


Figure-C12: Average intensity distribution along the lines versus time for 24% sample at various shear rates, obtained from Figure-C11.

For samples under 24% of SDS+Water, the original images, Fourier transform images, plots of intensity distribution for the ring and the lines are all similar at the same shear rate. However, for samples over 24%, the above patterns are different at lower shear rate because the higher concentrated lyotropic lamellar phase will not transition to MLV orientation state at lower shear rates. To give an example, the results for the 30% sample at shear rate $3.3s^{-1}$ are shown in Figure-C13. The image for the sample between crossed polarizers shows that the final state is not a uniform multi-lamellar vesicle structure, and it contains lots of defects in the flow direction. Because the sample has a large thickness when compared to the depth of focus of the camera, it is not easy for us to analyze what the actual structure of the liquid is.

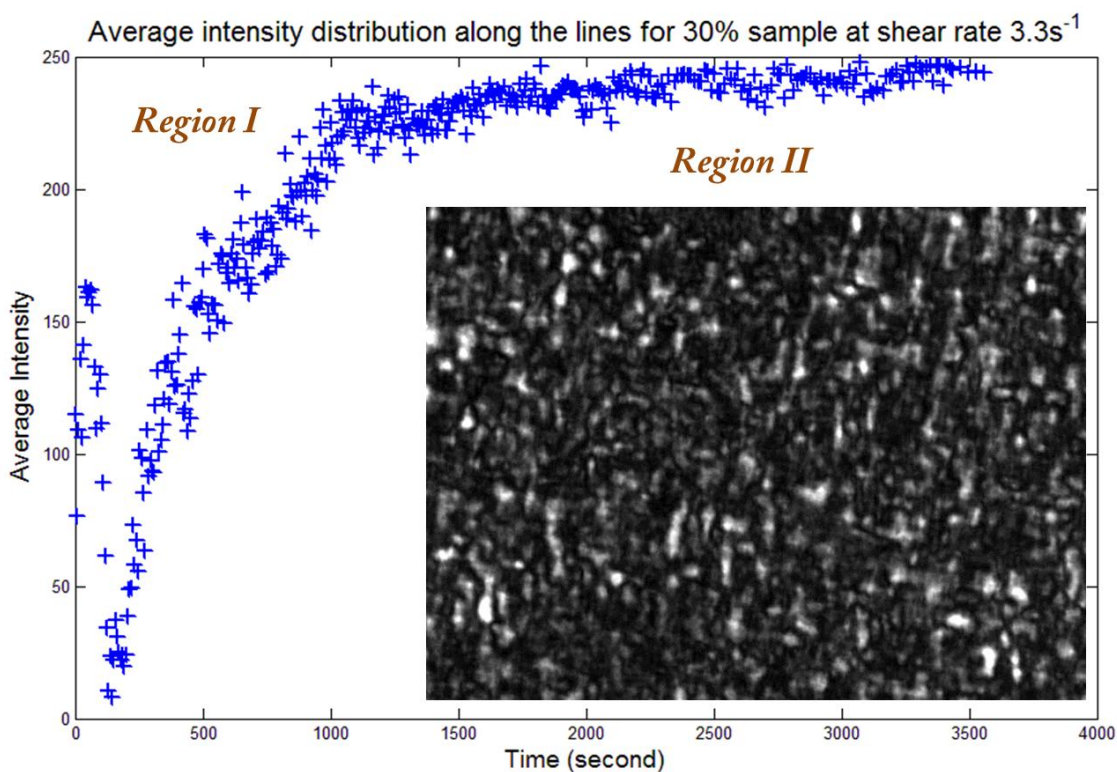


Figure-C13: Average intensity distribution along the lines plot for 30% sample at shear rate $3.3s^{-1}$ and one typical image at *Region II*.

For thick samples at low shear rate, the lamellar phase cannot reach to the uniform MLV orientation state, so there is no second transition during shearing.

3-4 Transition Time for Different Samples under Various Shear Rates

Based on the procedure of Fourier transform analysis for images, we are able to get the transition time for all the samples at different shear rates.

From Figure-C14 and Figure-C15, the qualitative relation between the first transition time and concentration of surfactant or shear rate will be obtained. For the same shear rate: the higher the concentration, the faster the lamellar phase transits from *Region I* to *Region II*. On the other hand, for the same concentration of surfactants, the higher the shear rate, the faster the lamellar phase transits from *Region I* to *Region II*. Besides, during the first transition time, dilute lyotropic lamellar phases show abrupt changes, and concentrated solutions show us smooth and slight changes.

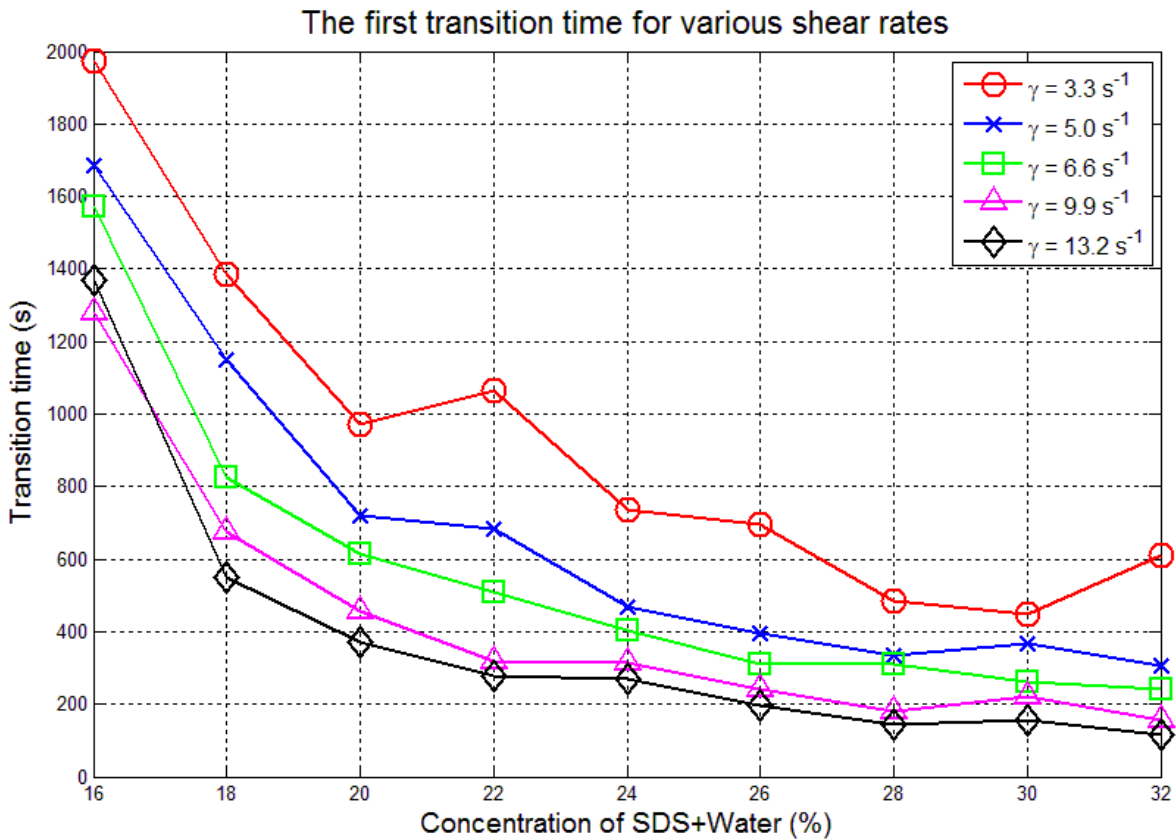


Figure-C14: The first transition time versus concentration of SDS+Water for different shear rates.

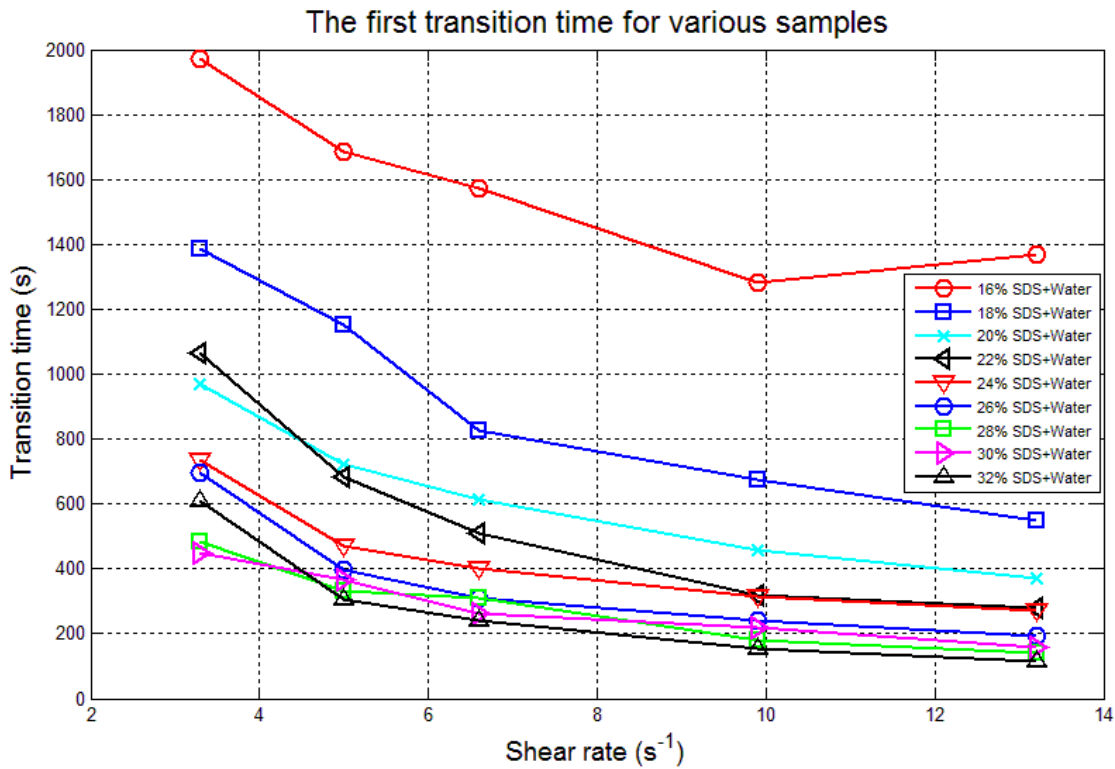


Figure-C15: The first transition time versus shear rate for different concentrated samples.

We have the same plot for the second transition time, as shown in Figure-C16.

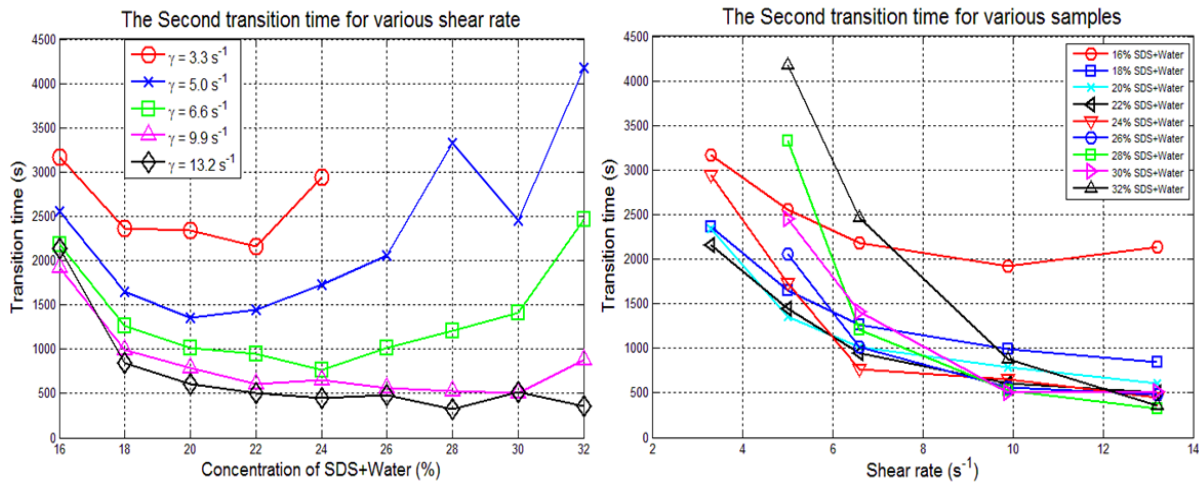


Figure-C16: The plots of the second transition time against both: concentration of SDS+Water, and shear rates.

For the second transition time, the rule that the increase of shear rate will hasten the transition from *Region II* to *Region III* is also followed. However, it does not quite follow the rule that higher concentration of surfactant will speed up the transition, especially for the dilute solution.

As observed in Figure-C16, the second transition does not exist for samples over 26%. This phenomenon is consistent with the orientation diagram for Water-Pentanol-Dodecane-SDS system, where higher concentrated lamellar phase cannot reach the multi-lamellar vesicle state at a lower shear rate [4].

Region II is a mixture of Region I and Region III, and the time interval of Region II is plotted in Figure-C17.

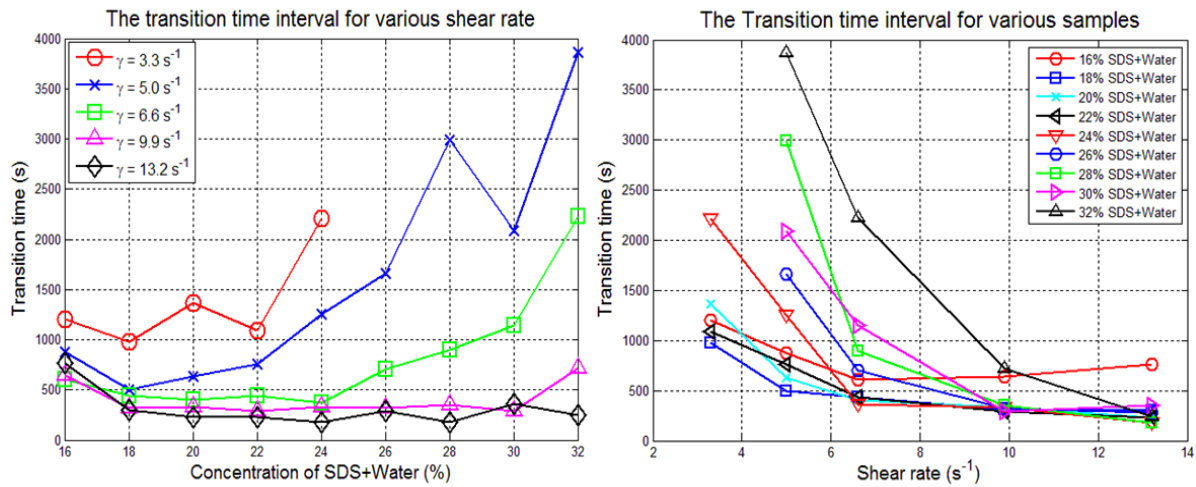


Figure-C17: The plots of the time interval for *Region II* against both: concentration of SDS+Water, and shear rate.

Therefore, the *Region II* time interval basically follows the rules for the second transition time.

3-5 Uncertainty of the Results

All results were obtained under the same conditions, such as room temperature and fixed disk separation, to maintain the consistency. To ensure the results we obtained were valid and reasonable, we needed to test the uncertainty and error. Therefore, more experiments on two different samples with concentration of 16% and 24% of SDS+Water under the same five shear rates were executed and the transition times are shown in Table-D2.

shear rate	Sample with 16% SDS+Water					Sample with 24% SDS+Water				
	t1-#1	t1-#2	avg(t1)	$\Delta t1$	$(\Delta t1)\%$	t1-#1	t1-#2	avg(t1)	$\Delta t1$	$(\Delta t1)\%$
3.3	1602	1972	1787	370	20.7	595	736	666	141	21.2
5	1683	1684	1684	1	0.1	397	470	434	73	16.8
6.6	1394	1572	1483	178	12.0	285	403	344	118	34.3
9.9	1261	1281	1271	20	1.6	205	315	260	110	42.3
13.2	1352	1368	1360	16	1.2	176	270	223	94	42.2
	t2-#1	t2-#2	avg(t2)	$\Delta t2$	$(\Delta t2)\%$	t2-#1	t2-#2	avg(t2)	$\Delta t2$	$(\Delta t2)\%$
3.3	2874	3173	3024	299	9.9	2535	2947	2741	412	15.0
5	2712	2559	2636	-153	-5.8	1215	1727	1471	512	34.8
6.6	2407	2177	2292	-230	-10.0	782	769	776	-13	-1.7
9.9	2181	1923	2052	-258	-12.6	528	649	589	121	20.6
13.2	2673	2135	2404	-538	-22.4	369	450	410	81	19.8

Table-D2: Transition times for samples with 16% and 24% of SDS+Water in two trials. Here, t1, t2 represents the first transition time and the second transition time in seconds respectively. #1 & #2 represents the first trial and second trial respectively.

From the repeat experiments, we can get some ideas about the reproducibility of the results that have been obtained. As for the first transition time and the second transition time for the 16% sample, the maximum tolerance is $\pm 11\%$, and most of them are under $\pm 6\%$, which is very convincing. However, for the 24% sample, there are two points which are far away from the average value, and the tolerances are about $\pm 20\%$ at shear rate of $9.9s^{-1}$ and $13.2s^{-1}$ for the first transition time, and two more points have a $\pm 17\%$ error. The results for the 16% sample are more believable than the results for the 24% sample.

The uncertainty may come from the following reasons: the samples are not totally uniform, the background environment may produce random influences, two disks are not totally flat and parallel, and the method of getting transition time is a little subjective. For the accepted tolerances, most of the uncertainties do not exceed $\pm 15\%$ which is a reasonable tolerance for our results.

All original data and results are stored on the hard drive and can be traced and tested.

IV. DISCUSSION

1. Formation and Evolution of Multi-lamellar Vesicle

Many videos are recorded to show how one single multi-lamellar vesicle is being followed over the course of several minutes, and the purpose is to see how the structure is formed from the lamellar phase and how it changes over time.

Theoretically, if one particle is captured in the field of view, we can adjust the relative speed of two disks properly, and then the particle will be stabilized in both radius direction and tangential direction. However, the particle will still be moving slowly and randomly. The reason for this situation is that the two transparent glass disks are not perfectly parallel to each other and their thickness has some minor tolerance.

Even though one multi-lamellar vesicle can be observed and followed for more than twenty minutes, the process of formation of one single multi-lamellar vesicle from lamellar phase still remains unknown. We cannot predict where the multi-lamellar vesicle will appear, so it is not possible to observe and determine the molecular structure before it forms into a multi-lamellar vesicle. The evolution of one single multi-lamellar vesicle over time still remains as a mystery since the shape and size of the followed multi-lamellar vesicle remains the same over the course of 20 minutes.

Previous work from Roux and co-workers shows that the size of multi-lamellar vesicles is proportional to the reciprocal of the square root of the shear rate, so the size or shape for one single multi-lamellar vesicle may be related to the shear rate. If we could keep tracking one multi-lamellar vesicle while changing the shear rate at the same time, the dependence of the multi-lamellar vesicle on shear rate can be acquired.

2. Transition Time for Lamellar Phase under Shear

Although the development of one single multi-lamellar vesicle cannot be determined, we are able to observe the transition progress from the real images and obtain the transition time between different orientation states when the lamellar phase is under shear.

It will take some time for the lamellar phase to transition from the original orientation state to the multi-lamellar vesicle state, and the duration varies for different shear rates. As we have discovered, there are three main regions from the initial lamellar phase to the final uniform multi-lamellar vesicle state when it is under shear. *Region I* shows lots of defects in the flow direction, while *Region III* is the uniform state that only contains multi-lamellar vesicles, and finally *Region II* is a mixture of both *Region I* and *Region III*. The process of transition from lamella to vesicle is slow and smooth, and *Region II* is the transition interval between the two structures.

By applying the Fourier transformation analysis on the images, the transition time for lyotropic lamellar phase with different concentration of surfactant under various shear rates can be calculated. The results show us that the transition time between *Region I* and *Region II* will be reduced by increasing either concentration of surfactant or shear rate, but the second transition time does not follow these rules.

During the shearing process, the brightness and observability of the image may change because the lamellar phase structure is changing, so we adjusted the exposure time and gain for the camera to get a better view. In spite of changing the parameters of the camera, the spatial frequency information contained in the images will remain the same, which will also remain the same for the Fourier transformation images. This is the reason why we can chose this new method to analyse the images and the transition time.

It is unavoidable that small dust or impurities are mixed into our Water-Pentanol-Dodecane-SDS lamellar solutions since the glass disks are not super clean, and the sample preparation procedure is not perfectly pollution-immune. Some unwanted foreign substances have come into the field of view and were captured by the camera. It is necessary to note that these images containing impurities or air bubbles were discarded and not included in our analysis. The number of these images is no more than 5% of the total number of images. However, the images are recorded according to the real date and time, so discarding a reasonable quantity of unwanted images will neither change the time difference between images, nor affect our results.

As shown in Figure-G8 and Figure-G11, the intensity plot along a ring on the Fourier transformed images has a bright line at angle $\pi/2$ and $3\pi/2$ rad. This line is due to the algorithm of the Fast Fourier Transform in Matlab, but it does not influence the main part of the Fourier transform image. Therefore we chose the wide lines at the angle smaller than $\pi/2$ and larger than $3\pi/2$ to get the average pixel value.

When looking for the transition points from the intensity plot of the lines, we draw two basic fitting lines to obtain the intersection and middle point. This is more or less subjective because the fitted lines are based on the points that we choose, and this increases the uncertainty of the final transition time. In addition, the transition time is not the absolute point that separates the two different regions abruptly, but the relative time when the structure of lamellar phase is changing gently. For example, from the first transition time, more multi-lamellar vesicles show up as time goes forward, but more defects along flow direction appear as time travels backward.

We have determined the transition time for nine samples with different concentrations under five low shear rates, and the results have revealed some qualitative relations between the transition time and the concentration of SDS+Water for each shear rate. The data is not sufficient to get the quantitative relationship unless we use a larger variation of concentrated samples and more shear rates. As to the uncertainty of the transition time, we did two trials for the 16% and the 24% sample under the same five shear rates, and found that the error was less than $\pm 15\%$, which is a reasonable tolerance.

Moreover, as we discussed before, all the experiments were performed at room temperature (about 21°C) which is a very important parameter for chemical substances. If the temperature could be controlled, we could explore the transition time or other properties over time. The distance between the two disks has been kept as 0.254 millimeter, and this is also an important variable which needs to be tested.

3. Further Study

Samples with higher concentration of surfactant, as well as higher shear rates, should be introduced into the experiment to explore whether there could be a qualitative relationship

between transition time and concentration or shear rate. Also, more trials on the samples that we already used should be tried again to obtain the data with higher accuracy.

Changing the gap between the two disks but keeping the same shear rates could be a further study on whether the separation may have an influence on the transition time. As well, a temperature control could be added to the system to maintain the experiment in a thermostatic environment.

Limited by the current set-up, we were unable to acquire the size of the multi-lamellar vesicle on the image unless it was very big, but the dimensional information is essential if we want to verify the influence made by shear rate. Thus, an approach of obtaining the size of the multi-lamellar vesicle could be helpful for us to obtain a more detailed relationship between shear rate, transition time, concentration of SDS+Water, and the size of multi-lamellar vesicle when a lyotropic lamellar phase is under shear.

V. CONCLUSION

In this exploration of Water-Pentanol-Dodecane-Water lyotropic lamellar phase under shear flow, some interesting discoveries have been acknowledged.

Firstly, we can follow one particle for a long time in a Couette shear flow between two transparent co-rotational disks through microscope, camera, motor controls and LabView software. In this case, the followed particle is a multi-lamellar vesicle under simple polarizing microscope, and we found that one single multi-lamellar vesicle does not have any obvious change as time goes on. In multi-lamellar vesicle orientation state, not only vesicles with small size less than 10 micrometers were observed, but also large multi-lamellar vesicles that were easily to be followed.

Then, when a moderate shear rate is applied to a lamellar phase, three regions are discovered to take the lamellar phase from the original state to the multi-lamellar vesicle orientation state.

Region I is the state where lots of defects are exist in the shear direction, *Region III* is the uniform multi-lamellar vesicle orientation state, and *Region II* is a mixture of *Region I* and *Region III*.

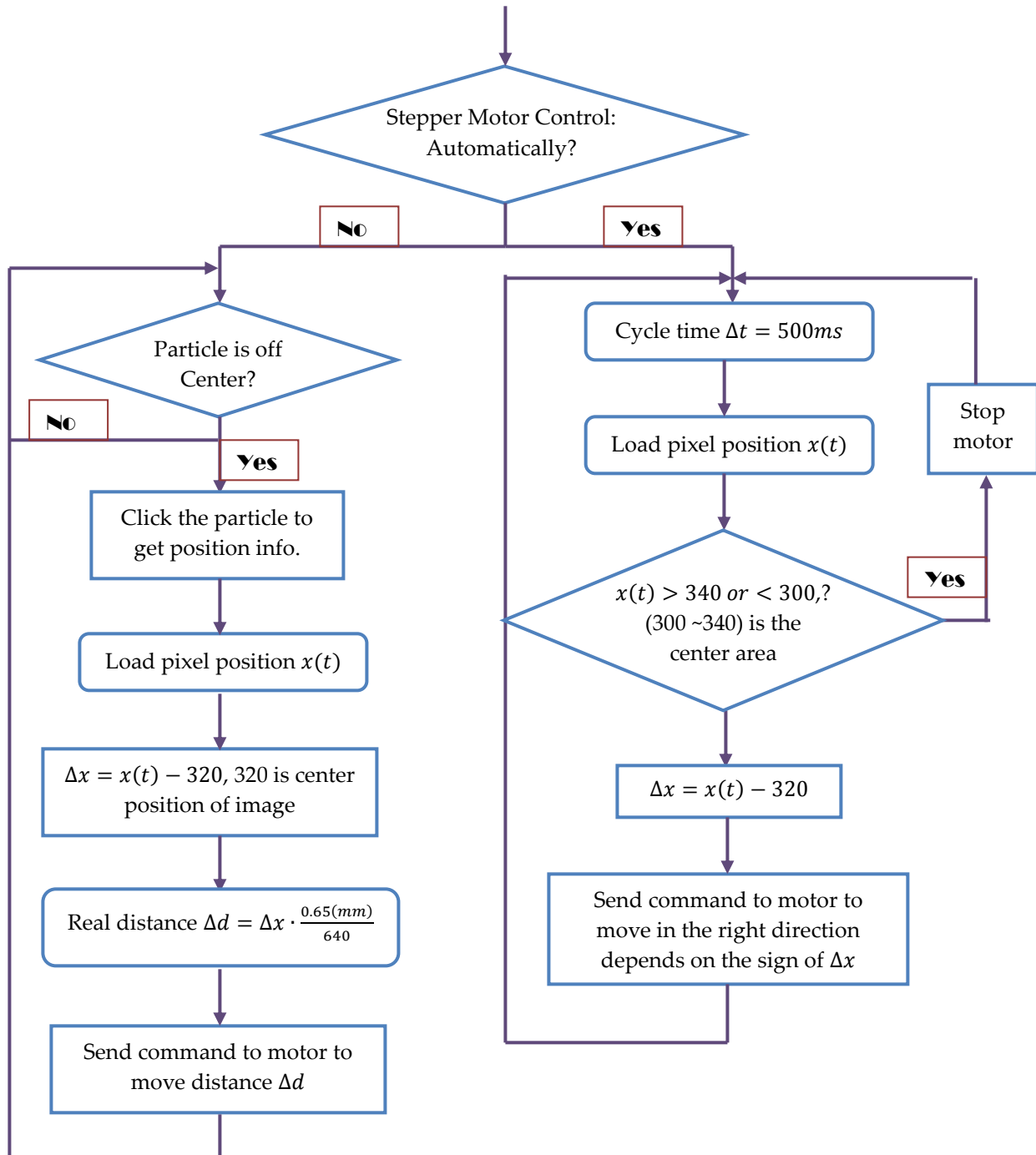
In addition, the relation among transition time, different regions, shear rate, and concentration of surfactant is qualitative obtained. Both the first transition between *Region I* to *Region II* and the second transition between *Region II* to *Region III* can be accelerated by increasing the shear rate. However, only the first transition time decreases if the concentration of SDS+Water is increasing, and the more dilute the lamellar phase is, the more abruptly first transition happens between adjacent concentrations. Furthermore, for higher concentrated lamellar phases at low shear rate, the second transition does not exist since they cannot reach to the multi-lamellar vesicle orientation state.

REFERENCES

- [1] R.G. Larson, *The Structure and Rheology of Complex Fluids*, Oxford University Press, New York, (1999).
- [2] G.J. Sharpe, *Fluid Flow Analysis*, Heinemann Educational Books Ltd., London, (1967).
- [3] R.P. Chhabra, J. F. Richardson, *Non-Newtonian Flow and Applied Rheology, 2nd edition*, Elsevier Ltd., Burlington, (2008).
- [4] O. Diat, D. Roux, F. Nallet, *Effect of shear on a lyotropic lamellar phase*, J. Phys. II France 3 (1993) 1427-1452.
- [5] O. Diat, D. Roux, *Preparation of monodisperse multilayer vesicles of controlled size and high encapsulation ratio*, J. Phys. II France 3 (1993) 9-14.
- [6] W. F. Brinkman, P.E. Cladis, *Defects in liquid crystals*, Physics Today 35 (1982) 48.
- [7] O.D. Lavrentovich, *Defects in liquid crystals: surface and interfacial anchoring effects*, Patterns of Symmetry Breaking, Springer Netherlands, (2003) 161-195.
- [8] C.Y. Lu, *Sizes of Multilamellar Vesicles in Shear*, Physical Review Letters 109 (2012) 128304.
- [9] D. Roux, *Rheophysics of lamellar phase*, Institut François du Pétrole, Pessac, (1997).
- [10] P.J. Collings, *Liquid Crystals*, Princeton University Press, Princeton, New Jersey, (1990).
- [11] M. Daoud, C.E. Williams, *Soft Matter Physics*, Les Editions de Physique, (1995).
- [12] B.S. Massey, J. Ward-Smith, *Mechanics of Fluids, 9th edition*, Spon Press, London and New York, (2012).
- [13] D. Roux, J. Leng, A. Colin, A.S. Wunenburger, *Dynamics of lamellar phase under shear*, AIP Conference Proceedings, Vol. 469, p. 93, (1999).
- [14] G. Pelzl, A. Hauser, *Birefringence and phase transitions in liquid crystals*, Phase Transitions, Vol.37, p. 33-62, (1991).
- [15] L. SOUBIRAN, C. COULON, P. SIERRO, D. Roux, *Conductivity and Dielectric Measurements of a Lyotropic Lamellar Phase under Shear Flow*, EPL (Europhysics Letters) 31.4 243 (1995).
- [16] O. Diat, D. Roux, F. Nallet, *Lamellar phase under shear: SANS measurement*, Le Journal de Physique IV 3.C8-193 (1993).
- [17] A.D. McNaught, A. Wilkinson, *IUPAC Compendium of Chemical Terminology*, International Union of Pure and Applied Chemistry, Zurich, (1997).

- [18] P. Le Gal, Y. Tasaka, J. Nagao, A. Cros, K. Yamaguchi, *A Statistical Study of Spots in Torsional Couette Flow*, Journal of Engineering Mathematics, 57, 289 (1997).
- [19] S.H.J. Idziak, S.E. Welch, M. Kisilak, C. Mugford, G. Potvin, L. Veldhuis, E.B. Sirota, *Undulating Membrane Structure Under Mixed Extensional-Shear Flow*, European Physical Journal E, 6, 139(2001).
- [20] G. Mazzanti, S.E. Guthrie, E.B. Sirota, A.G. Marangoni, S.H.J. Idziak, *Orientation and Orientation and Phase Transitions of Fat Crystals Under Shear*, Crystal Growth & Design, 3, 721(2003).
- [21] S.E. Friberg, P. Bothorel, *Microemulsions: Structure and Dynamics*, CRC Press, Florida, (1987).
- [22] W. Niblack, *An introduction to digital image processing*. Strandberg Publishing Company, Denmark, (1985).
- [23] A.K. Jain, *Fundamentals of digital image processing*, Englewood Cliffs, Prentice-Hall, (1989).
- [24] C. Solomon, T. Breckon, *Fundamentals of Digital Image Processing: A practical approach with examples in Matlab*. John Wiley & Sons Ltd., Chichester, (2011).
- [25] R.W. Fox, A.T. MacDonald, P.J. Pritchard, *Introduction to Fluid Mechanics, 6th edition*, John Wiley & Sons Inc., (2004).
- [26] B. Jönsson, B. Lindman, K. Holmberg, B. Kronberg, *Surfactants and Polymers in Aqueous Solution*, John Wiley & Sons Ltd., Chichester, (1998).
- [27] R.H. Sabersky, A.J. Acosta, E.G. Hauptmann, *Fluid Flow: A first course in fluid mechanics, 3rd edition*, Macmillan publishing company, New York, (1989).
- [28] H.J. Stewart, *The Energy Equation for A Viscous Compressible Fluid*, Proceedings of the National Academy of Sciences of the United States of America 28.5 161 (1942).
- [29] J.B. Kelley, *The Extended Bernoulli Equation*, American Journal of Physics, 18, 202, (1950).
- [30] M.G. Berni, C.J. Lawrence, D.Machin, *A review of the rheology of the lamellar phase in the surfactant system*, Advances in colloid and interface science 98.2 217-243 (2002).
- [31] J.S. Allen, *A model for fluid flow between parallel, co-rotating annular disks*, Doctoral dissertation, University of Dayton, (1990).
- [32] M.T. Shaw, Z. Liu, *Single-point determination of nonlinear rheological data from parallel-plate torsional flow*, Applied Rheology 16.2 70-79 (2006).

Appendix I



Appendix II

